A&A, 715, A195 (2026)
https://doi.org/10.1051/0004-6361/202661200
© The Authors 2026

Astronomy & Astrophysics

SN 2019vxm: A luminous and long-lived Type IIn supernova with early flash-ionisation features

Y.-Z. Cai (蔡永志), A. Pastorello, T. J. Moriya, X.-F. Wang (王晓锋), A. Reguitti, A. V. Filippenko, L. Tomasella, K. Čotar, et al.

(Full author list and affiliations details can be found after the references)

Received 29 May 2026 / Accepted 28 July 2026

ABSTRACT

We present the photometric and spectroscopic analysis of the luminous and long-lasting Type IIn supernova (SN) 2019vxm. The SN reaches a peak V-band absolute magnitude of $M_V = -20.01 \pm 0.13$ mag in 35.0 days and displays slow evolution in both the light curves and spectra, resembling those of long-lived SNe IIn. A mid-infrared excess is detected starting from seven months after maximum brightness, suggesting a few 10^{-3} $M_\odot$ of dust are newly formed at $\gtrsim$210 days (and up to 0.01 $M_\odot$ at +4.5 yr). The spectra are dominated by a blue continuum at early stages, with narrow, symmetric Balmer lines and flash-ionisation emission lines of C III, N III, and He II. Comparing our flash-ionised spectrum with early interacting SN spectral models, we estimate a lower limit for the mass-loss rate of the progenitor of $\dot{M} \gtrsim 10^{-2}$ $M_\odot$ yr^{-1}. A weak P Cygni absorption feature is detected in the Hβ profile of the high-resolution Echelle spectrum at +19.7 d, suggesting the presence of slow-moving (60 ± 10 km s^{-1}), unshocked circumstellar material (CSM) arising from the pre-SN wind of the progenitor. The Hα and Hβ profiles gradually evolve and become broader and asymmetric, showing a progressively increasing blueshift, with a clear flux deficit in the red wings of the broad velocity component after +102 days. Our observed bolometric light curve before ~100 days can be well fitted by a power-law function ($L(t) = 2 \times 10^{44}(t/\mathrm{day})^{-0.49}$ erg s^{-1}), which is very similar to SN 2010jl. The bolometric luminosity evolution indicates that the progenitor mass-loss rate was ~0.02–0.04 $M_\odot$ yr^{-1} if we assume $\rho_{\rm CSM} \propto r^{-2}$ and the wind velocity of 60 km s^{-1}. These findings are consistent with an asymmetric, dense circumstellar environment, indicative of a massive, compact progenitor such as a luminous blue variable (LBV) embedded in a clumpy, asymmetric medium. However, we cannot entirely rule out an extreme red supergiant (RSG) with superwinds or a transitional post-RSG/LBV star as the potential progenitor.

Key words. circumstellar matter – supernovae: general – supernovae: individual: SN 2019vxm

1. Introduction

Type IIn supernovae (SNe IIn) were first introduced by Schlegel (1990) (but see also Filippenko 1989 for earlier examples) to describe a subclass of hydrogen-rich SNe characterised by relatively narrow hydrogen emission lines, ranging from ~100 to ~1000 km s^{-1}, superposed on a blue continuum in their early-time spectra (see Filippenko 1997 for a review). These emission lines indicate the presence of a slowly expanding circumstellar medium (CSM). The interaction between the rapidly expanding SN ejecta and the CSM generates a forward shock that propagates into the CSM and a reverse shock that moves into the ejecta (see e.g. Chevalier & Fransson 1994; Chugai 1997). The presence of ejecta-CSM interaction is revealed by typical observables such as strong X-ray and radio emission, a blue spectral continuum, and multicomponent line profiles, sometimes with boxy components (see e.g. Fraser 2020; Dessart & Hillier 2022; Dessart 2024; Gangopadhyay 2024).

Type IIn SNe are relatively rare, representing around 10% of all core-collapse (CC) SNe in the local Universe (Smartt 2009; Smith et al. 2011a; Li et al. 2011; Cappellaro et al. 2015; Perley et al. 2020; Ma et al. 2025a,b), but Cold & Hjorth (2023) presented a lower rate estimate of around 5%, and Eldridge et al. (2013) even estimated a much lower rate of 2.4%. Type IIn SNe display tremendous heterogeneity in their light curves and spectra (see e.g. Kiewe et al. 2012; Pastorello et al. 2019; Nyholm et al. 2020; Reguitti et al. 2024; Ransome & Villar 2025; Salmaso et al. 2025), with absolute magnitudes at peak ranging from $M_r \approx -16$ mag for the faintest events to $M_r \approx -22$ mag for very luminous objects (e.g. Nyholm et al. 2020; Hiramatsu et al. 2026). The light-curve shapes are divided into three main subgroups on the basis of their morphology (Taddia et al. 2013, 2015): the plateau-like SNe IIn-P (e.g. Kankare et al. 2012; Mauerhan et al. 2013; Elias-Rosa et al. 2024), the fast and linearly (in magnitudes per day) declining SNe IIn-L (e.g. Fassia et al. 2000; Di Carlo et al. 2002; Pastorello et al. 2002), and the long-lasting SNe IIn (e.g. Turatto et al. 1993; Zhang et al. 2012; Stritzinger et al. 2012; Tartaglia et al. 2020; Moran et al. 2023). Members of this last category are generally more luminous than SNe IIn-P, although without reaching the brightness of superluminous (SL) SNe.

In addition, several studies suggest that SNe IIn may be more prone to containing warm dust compared to other types of CC SNe, as they typically exhibit late-time ($\gtrsim$100 days) infrared (IR) emission associated with warm dust (e.g. Fox et al. 2009, 2010, 2011; Miller et al. 2010a,b; Maeda et al. 2013; Gall et al. 2014; Bevan et al. 2019, 2020; Dwek et al. 2021; Baer-Way et al. 2025; Shahbandeh et al. 2025). This photometric diversity, along with spectral information such as CSM and ejecta velocities, reflects a wide range of CSM geometric configurations, masses, and density profiles – hence, in general, the different properties of the progenitors and their local environments.

The variety of SN IIn observables suggests the existence of multiple progenitor channels (see e.g. Dwarkadas 2011; Moriya et al. 2013b; Leloudas et al. 2015; Smith 2017; Ransome & Villar 2025). In particular, luminous blue variables (LBVs) have been proposed as plausible progenitors by Kotak & Vink (2006), Gal-Yam et al. (2007), and Gal-Yam & Leonard (2009), as they expel significant amounts

Open Access article, published by EDP Sciences, under the terms of the Creative Commons Attribution License (https://creativecommons.org/licenses/by/4.0), which permits unrestricted use, distribution, and reproduction in any medium, provided the original work is properly cited.
This article is published in open access under the Subscribe to Open model. Subscribe to A&A to support open access publication.

of mass during their eruptive phases at velocities comparable to those observed in the spectra of SNe IIn (Kiewe et al. 2012; Taddia et al. 2013). Specifically, this scenario is strongly supported by the direct identification of the progenitor of the Type IIn SN 2005gl in pre-explosion Hubble Space Telescope (HST) archival images and its subsequent disappearance in late-time observations of the SN site (Gal-Yam et al. 2007; Gal-Yam & Leonard 2009). Furthermore, the direct identification of progenitor stars in a few additional cases, such as SN 2009ip (Smith et al. 2010; Foley et al. 2011), SN 2010jl (Smith et al. 2011b), SN 2010bt (Elias-Rosa et al. 2018), and SN 2015bh (Elias-Rosa et al. 2016; Thöne et al. 2017), reinforces the connection between SNe IIn and LBVs. On the other hand, the class of SN 2008S-like objects[1] exhibits relatively narrow hydrogen lines similar to those of SNe IIn, and their progenitors are typically enshrouded in dusty cocoons and have modest estimated initial masses of 8–15 $M_\odot$ (e.g. Prieto et al. 2008; Cai et al. 2018, 2021; Valerin et al. 2025a,b). While Smith et al. (2009a) interpreted these events as SN impostors analogous to the eruptions of LBVs, alternative explanations – such as a super asymptotic giant branch (AGB) stars (e.g. Moriya et al. 2014) or blue supergiants (BSGs; Moriya & Menon 2024) as progenitors – remain plausible.

On the other hand, the most extreme exemplars, such as overluminous and long-lasting events, significantly broaden our understanding of SNe IIn. For instance, superluminous SNe IIn require both a high kinetic energy in the inner shell and a large mass reservoir in the outer shell (see e.g. Moriya et al. 2013a; Dessart et al. 2015). Some good examples of such SNe IIn are SN 2008am (Chatzopoulos et al. 2011), SN 2010jl (e.g. Andrews et al. 2011; Stoll et al. 2011; Smith et al. 2011b, 2012; Zhang et al. 2012; Maeda et al. 2013; Ofek et al. 2014, 2019; Fransson et al. 2014; Jencson et al. 2016; Chugai 2018; Niu et al. 2024), SN 2015da (Tartaglia et al. 2020; Smith et al. 2024), and more recently SN 2017hcc (e.g. Prieto et al. 2017; Smith & Andrews 2020; Moran et al. 2023; Sethulakshmi et al. 2026). In this study, we present observations of the luminous, slowly evolving Type IIn SN 2019vxm, monitored for more than two years. Relevant datasets for this SN have been published by Vallely et al. (2021), Tsvetkov et al. (2023, 2024), Lane et al. (2026), and Lelkes et al. (2026) and are discussed later.

This paper is structured as follows. In Sect. 2, we describe the basic information on SN 2019vxm, including discussions of distance and reddening. The photometric and spectroscopic analysis are presented in Sects. 3 and 4, respectively. In Sect. 5, we discuss our results. We report all the photometric and spectroscopic observations as well as the data-reduction techniques in Appendix A.

2. Basic information for SN 2019vxm

SN 2019vxm (also known as ASASSN-19acc, ATLAS19bchy, Gaia19fje, and PS20nyb) was first announced by the All-Sky Automated Survey for Supernovae (ASAS-SN; Shappee et al. 2014; Kochanek et al. 2017) on 2019 December 1 UTC (JD = 2 458 818.54; UTC dates are used throughout the paper), at $g \approx 15.4$ mag (AB mag; Oke & Gunn 1983) (Stanek 2019). The source was later classified by Leadbeater (2019) as a young Type IIn SN based on the similarity of its spectrum to that of SN 1998S about 20 days before maximum light. We remark that the classification criteria proposed by Leadbeater (2019) for SN 2019vxm are somewhat controversial, as SN 1998S is widely regarded as an intermediate case between flash-ionised Type II SNe and classical SNe IIn. In many hydrogen-rich SNe, early 'flash' features originate from the photoionisation of unshocked CSM by shock-breakout radiation and disappear within only a few days, indicating that the dense CSM is confined to the immediate environment of the exploding star (e.g. Khazov et al. 2016; Yaron et al. 2017; Bruch et al. 2021, 2023). The Type IIn classification of SN 2019vxm is confirmed by its subsequent photometric and spectroscopic evolution (see the following Sects. 3 and 4).

SN 2019vxm (RA = $19^{hr}58^{m}28^{s}.54$, Dec = +62°08′15″.83; J2000) has a projected offset of 3.19 kpc from the core of its possible host galaxy SDSS J195828.83+620824.3, and it is 8″.53 south and 2″.07 west of the galaxy centre (see Fig. A.1 in Appendix A.1). Given the absence of a published redshift for the putative host galaxy, we adopted $z = 0.019 \pm 0.001$ based on the fit to the early Hα emission line of SN 2019vxm, consistent with the value adopted by others (Leadbeater 2019; Tsvetkov et al. 2024; Lane et al. 2026). This redshift corresponds to a luminosity distance of $d_L = 79.2 \pm 4.2$ Mpc and a distance modulus of $\mu_L = 34.49 \pm 0.12$ mag. These values were calculated under the assumption of a standard Lambda Cold Dark Matter (ΛCDM) cosmology with $H_0 = 73\,km\,s^{-1}\,Mpc^{-1}$, $\Omega_M = 0.27$, and $\Omega_\Lambda = 0.73$ (Spergel et al. 2007).

The Milky Way (MW) extinction towards SN 2019vxm is $E(B-V)_{MW} = 0.087 \pm 0.002$ mag (Schlafly & Finkbeiner 2011), in agreement with the value inferred from the measurement of the equivalent width (EW) of the Galactic Na I D $\lambda\lambda$5890, 5896 absorption lines in our early, high-resolution ($R \approx 20\,000$) Copernico&Echelle spectrum taken on 2019 December 6 (+19.7 d after explosion). To estimate the additional host-galaxy extinction, we checked the EW of the interstellar Na I D absorption at the redshift of the host galaxy in the same spectrum but did not detect any Na I lines. This is consistent with the findings of Tsvetkov et al. (2023, 2024) in their better-quality spectra. The detailed identification of Na I D lines is shown in Fig. 1. Thus, we assumed that the total line-of-sight extinction of SN 2019vxm is equal to the Galactic value, $E(B-V)_{Total} = 0.087 \pm 0.002$ mag.

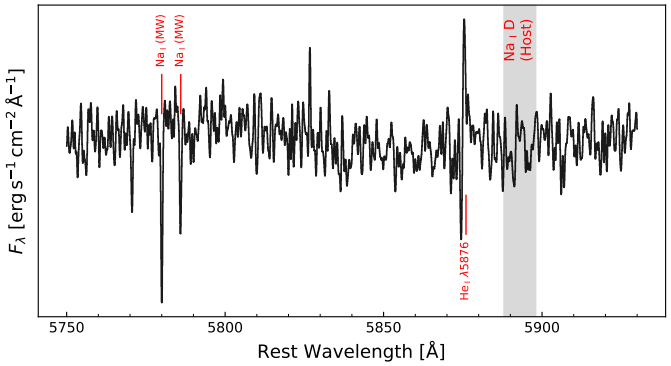


Fig. 1. Zoomed-in view of the Na I D spectral region in the Copernico&Echelle spectrum taken on 2019 December 06 (+19.7 d).

3. Photometry

We monitored the photometric evolution of SN 2019vxm for ~700 days from discovery in the optical band and for ~4 yr in the mid-infrared (MIR) domain. *Swift*-UVOT observations were obtained in the ultraviolet (UV) and the blue optical

[1] They are often referred to as intermediate-luminosity red transients (ILRTs; e.g. Botticella et al. 2009; Cai et al. 2022).

filters, spanning a period from ∼16 to 50 days after maximum light. The ground-based telescopes and instruments used in our photometric follow-up campaign are summarised as follows: the 0.67 m/0.92 m Schmidt telescope with a Moravian camera at Padova Astronomical Observatory, Istituto Nazionale di Astrofisica (INAF), Asiago, Italy; the 0.8 m Tsinghua-NAOC Telescope (TNT) at Xinglong Observatory, Hebei, PR China; the 0.8 m Joan Oró Telescope (TJO) equipped with LAIA camera located at Montsec Astronomical Observatory, Catalonia, Spain; the 1.02 m Nickel Telescope at Lick Observatory, California, USA; the 1.82 m Copernico Telescope with the Asiago Faint Object Spectrograph and Camera (AFOSC), hosted by INAF – Padova Astronomical Observatory, at the Asiago site, Italy; the 2.0 m Liverpool telescope (LT) equipped with the IO:O camera, located at Observatorio Roque de Los Muchachos, La Palma, Spain; the 2.4 m Lijiang Telescope with the Yunnan Faint Object Spectrograph and Camera (YFOSC) at Gaomeigu site, Lijiang Observatory (LJO), Yunnan, PR China; the 2.56 m Nordic Optical Telescope (NOT) with the Alhambra Faint Object Spectrograph and Camera (ALFOSC) at Observatorio Roque de Los Muchachos, La Palma, Spain. These facilities are also listed in Table B.1 (Appendix B). Furthermore, basic information on the photometric observations of SN 2019vxm and the data-reduction techniques are provided in Sect. A.2, while the multiband light curves are shown in Fig. 2.

3.1. Apparent magnitude light curves

We adopt an explosion time of MJD = 58804.03 ± 0.30, which was precisely constrained by (see their Fig. 1; Lane et al. 2026) using a broken power-law fit to the early, high-cadence Transiting Exoplanet Survey Satellite (TESS) light curve. We also adopt the *Swift* V-band rise time of $35.0^{+1.8}_{-1.7}$ d from (see their Table 1; Lane et al. 2026), which corresponds to a time of maximum at MJD ≈ 58839.0. For each UV band, the epoch of the first *Swift*-UVOT data point was adopted to estimate the decline slopes. Notably, the R- and I-band photometry of SN 2019vxm is concentrated around the peak luminosity and at phases later than 600 d (see Fig. 2); consequently, the decline slopes were computed only for these two bands at phases beyond 600 d.

The decline rates for different bands, summarised in Appendix Table D.2, exhibit a somewhat unexpected heterogeneity across the filters. After maximum light, SN 2019vxm displays a slow brightness decline with several changes in the decline rate. The UV light curves exhibit an approximately linear (in mag/day) decline, with rates significantly steeper than those in the optical bands (e.g. $\gamma_{0-40}(UVW2) \approx 4.96$ mag/100 d). Over the period 0–100 d after peak light, the blue optical filters fade more rapidly (e.g. $\gamma_{0-100}(B) \approx 1.32$ mag/100 d), whereas the redder ones evolve more slowly (e.g. $\gamma_{0-100}(r) \approx 0.61$ mag/100 d). Between 100 and 400 d, the decline rates in the optical bands decrease more slowly (e.g. $\gamma_{100-400}(r) \approx 0.25$ mag/100 d), indicating a plateau-like evolution. After 400 d, the decline rates increase again, approaching the ^{56}Co–^{56}Fe radioactive decay rate of 0.98 mag/100 d (e.g. $\gamma_{400-700}(r) \approx 0.83$ mag/100 d). As noted by Lelkes et al. (2026), this apparent alignment of the decline rate with the ^{56}Co–^{56}Fe slope is likely coincidental.

In the MIR domain, the light curves of SN 2019vxm exhibit a different evolutionary behaviour compared to those at shorter wavelengths (Fig. 2). The first *WISE* observation, taken at MJD ≈ 58810.94 (approximately 28 days before maximum light), yielded 2.5σ upper limits of $W1 \geq 14.7$ mag and $W2 \geq 14.4$ mag. However, the timing of the MIR peak is poorly constrained with the available MIR data. From the epoch of maximum in the V band, the MIR light curves may exhibit a peak within the first 0–200 d; however, the sparse sampling prevents a robust determination. Between 200 and 300 d, the luminosity remains approximately constant, and is followed by a second phase of brightening extending to ∼500 d. Meanwhile, the optical light curves show a pronounced decline, which may indicate the formation of dust (see Sect. 3.5 for a detailed discussion). Given the limited number of data points and the nonmonotonic evolution, we refrain from reporting quantitative rise or decline rates. Between 500 and 750 d, both the $W1$ and $W2$ bands show a declining trend, with decline rates of $\gamma_{500-750}(W1) \approx 0.21$ mag/100 d and $\gamma_{500-750}(W2) \approx 0.20$ mag/100 d. At later epochs, between 1000 and 1700 d, the MIR luminosity continues to decline. The decline rate in the $W1$ band increases slightly to $\gamma_{1000-1700}(W1) \approx 0.24$ mag/100 d, whereas that in the $W2$ band decreases to $\gamma_{1000-1700}(W2) \approx 0.12$ mag/100 d. Owing to the sparse data coverage at these late epochs, these estimates are subject to large uncertainties.

3.2. Absolute magnitude light curves

In this study, we compile a comparison sample of Type IIn SNe to serve as a reference for the photometric and spectroscopic analysis of SN 2019vxm. The comparison objects either have luminosities similar to the 'optical' luminosity of SN 2019vxm or a long evolution time. All comparison SNe, listed in Table D.1, are shown with their absolute V-band light curves in Fig. 3.

Using the distance and extinction values from Sect. 2, a second-order polynomial fit to the V-band light curve of SN 2019vxm yields a peak absolute magnitude of $M_V = -20.01 \pm 0.13$ mag at MJD = 58839.0 ± 1.7. While this luminosity is high in an absolute sense, it places SN 2019vxm at the fainter end of the comparison sample when SLSNe-IIn are included. Owing to their diverse progenitor channels and complex CSM interactions, Type IIn SNe exhibit a wide range of absolute magnitudes, spanning more than 6 mag (see e.g. Smith 2017; Nyholm et al. 2020; Hiramatsu et al. 2026; Ransome & Villar 2025). SN 2019vxm reaches a higher peak luminosity, approaching that of SNe 2010jl (∼−19.43 mag) and 2015da (∼−20.2 mag). Although it is not as luminous as SLSNe-IIn, SN 2019vxm exhibits a long-duration evolution similar to that of some extremely luminous SNe IIn (e.g. SNe 2003ma and 2017hcc). This is also consistent with the findings of Nyholm et al. (2020) that the most luminous SNe IIn are generally found to be longer lasting.

3.3. Colour evolution

The intrinsic colour evolution of SN 2019vxm, compared with those of the SN IIn comparison sample, is shown in Fig. 4. From ∼20 d before maximum light to ∼200 d after, the $B - V$ colour increases from ∼0.04 mag to a peak value of ∼0.87 mag, indicating an overall trend for the object to become redder with time. Such colour evolution alone does not uniquely imply a decrease in temperature, as dust extinction can preferentially attenuate blue photons and thus produce a redder observed colour. Moreover, line blanketing, which becomes more effective as the temperature decreases and the ionisation state of the ejecta evolves, can further enhance the reddening. In addition, the increasingly prominent Hα emission relative to the fading continuum may contribute to the observed increase in the $B - V$ colour through its contribution to the broadband V−band flux. At later phases, the $B - V$ colour remains relatively stable (∼0.67–0.80 mag).

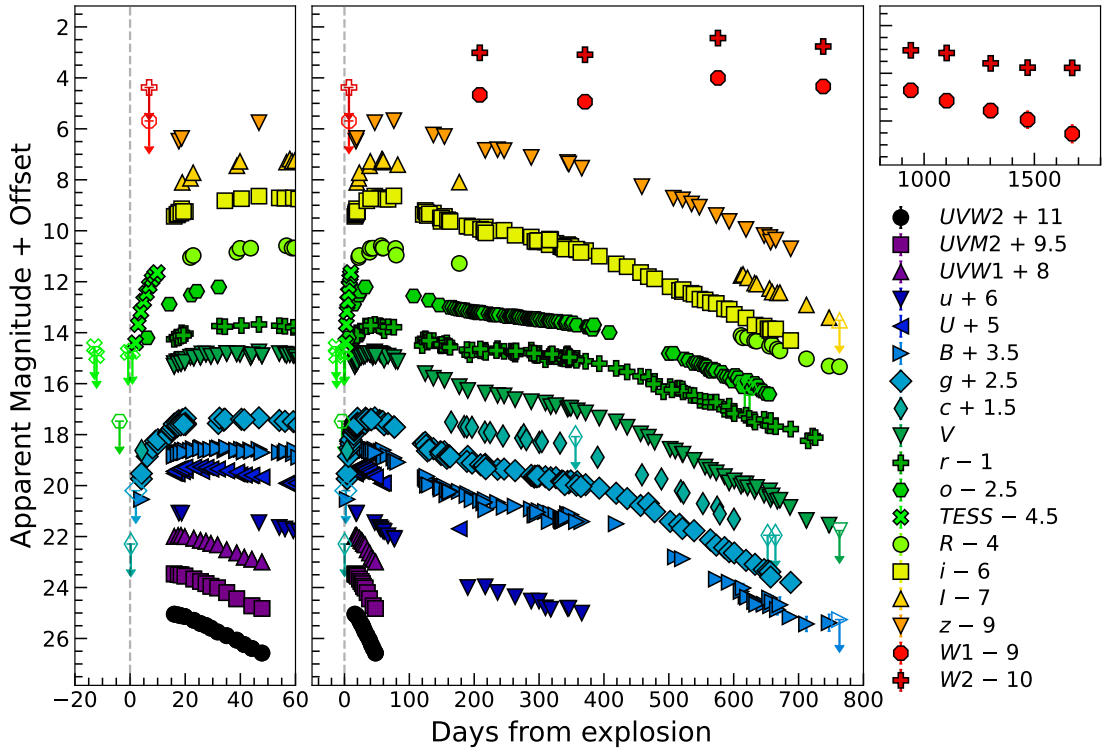


Fig. 2. Multiband (UV, optical, and MIR) apparent light curves of SN 2019vxm. Error bars are included for all photometric points, but the uncertainty is usually smaller than the marker size. A dotted vertical line indicates the explosion epoch.

Overall, the colour evolution of SN 2019vxm closely resembles that of SN 2017hcc. By contrast, the $B-V$ colour of SNe 2005ip and 2010jl remains relatively stable (∼0.30–0.50 mag) throughout the observed phases. The $B-V$ colour of SNe 2006tf and 2015da exhibits an increasing trend at early times; however, the $B-V$ colour of SN 2015da decreases after the peak before finally reaching a stable value.

In terms of the $r-i$ colour evolution, SN 2019vxm shows minor differences with respect to the other objects in the sample, particularly at phases later than 300 d (see the bottom panel in Fig. 4). From ∼20 d before maximum light to about 30 d after peak, the $r-i$ colour of SN 2019vxm increases from −0.18 mag to a peak value of ∼0.17 mag. Subsequently, the $r-i$ colour exhibits an apparent blueward trend, declining to ∼−1.53 mag by +700 d. This behaviour is likely driven by the increasing contribution of the Hα emission to the r band relative to the i band, rather than reflecting an intrinsic continuum evolution. In agreement with this interpretation, the $g-r$ colour shows a reddening trend over the same phases. The early evolution of SN 2019vxm within the first ∼400 d is broadly consistent with that of SN 2017hcc, although at later phases the $r-i$ colour of SN 2019vxm becomes noticeably bluer. For the other comparison Type IIn SNe, the $r-i$ colour evolution of SN 2015da and SN 2017hcc is broadly consistent, showing an initial reddening followed by a blueward trend and stabilising in the late phases. By contrast, the $r-i$ colour of SNe 2006tf and 2008am (Smith et al. 2008a; Chatzopoulos et al. 2011) remains nearly constant from the earliest epochs, whereas SN 2010jl exhibits blueward evolution after maximum light, although the late-time data are unavailable.

At late phases (>400 d), SN 2019vxm exhibits strong Hα emission that enhances the flux in the r band relative to the other bands, resulting in a progressively bluer $r-i$ colour. This strong Hα emission is usually associated with circumstellar interaction,

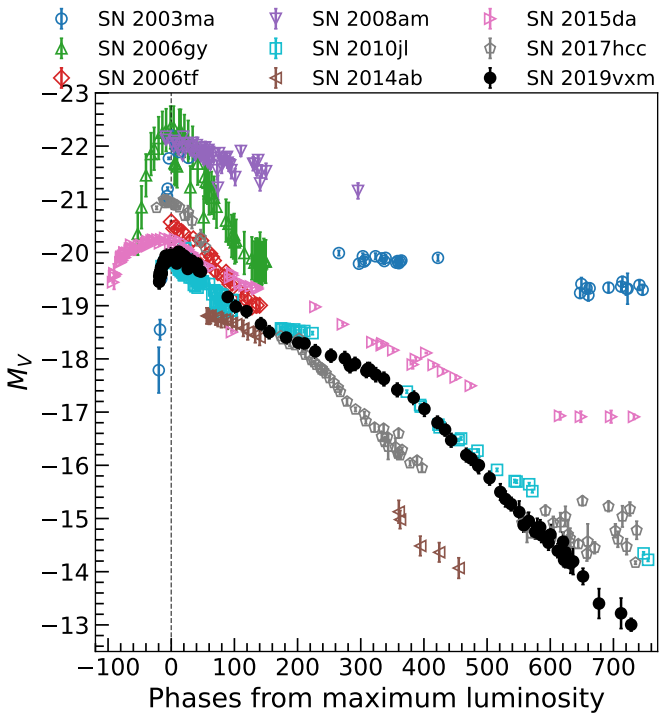


Fig. 3. Absolute V-band light curves of SN 2019vxm compared with those of bright Type IIn SNe and SLSN-II. For SNe 2006gy and 2008am, owing to the lack of sufficient V-band data, we use R- or i-band measurements instead.

suggesting that it may also be at play in SN 2019vxm during this stage. None of the comparison Type IIn SNe exhibit such a sustained blueward trend, although a similar behaviour was

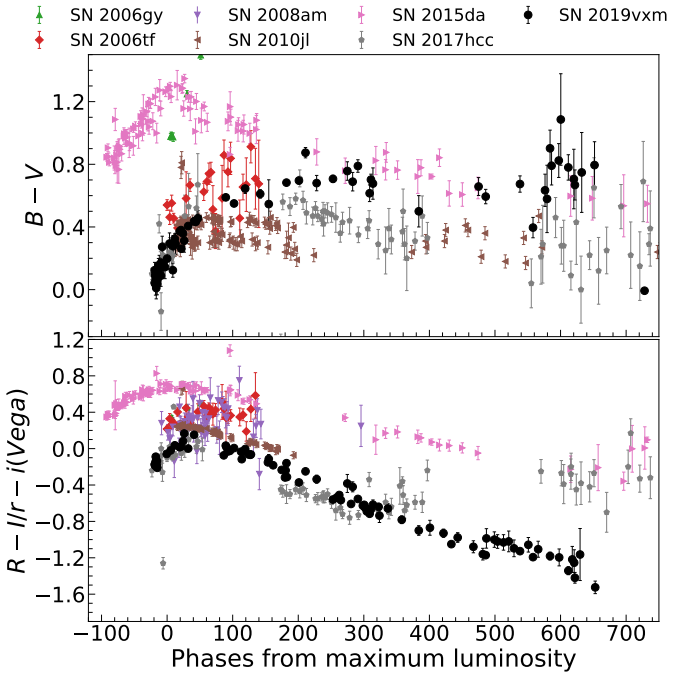


Fig. 4. Colour evolution of SN 2019vxm compared to a sample of SNe IIn. Upper panel: $(B-V)$ colour evolution. Lower panel: $(R-I)$ or $(r-i)$ colour evolution. The colour curves are corrected for both Galactic and host-galaxy extinction.

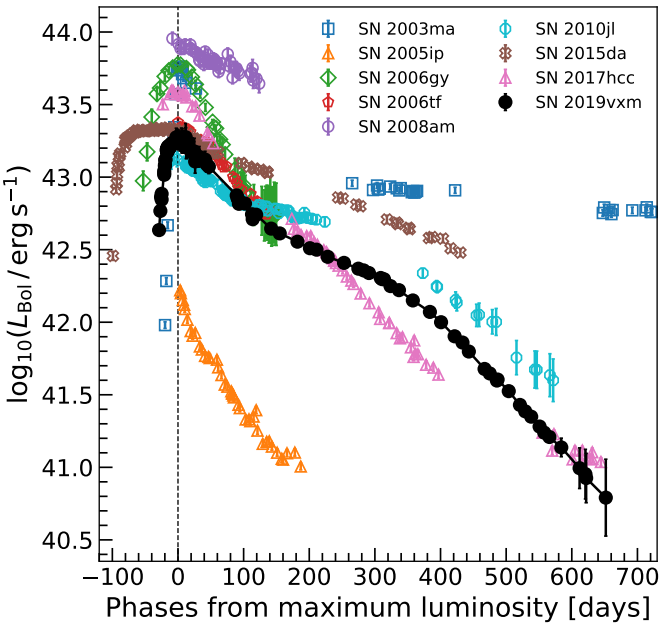


Fig. 5. Pseudobolometric light curves of SN 2019vxm and comparison bright SNe IIn and SLSN-II. The comparison objects either have luminosities similar to that of the 'optical' luminosity of SN 2019vxm or long evolution times. The luminosity has been calculated by integrating from the B to the I/i bands.

previously reported for other Type II SNe (e.g. SNe 2016iog and 2018hfm; Peng et al. 2026; Zhang et al. 2022), and attributed to the effects of CSM interaction.

3.4. Pseudobolometric light curves

To enable a meaningful comparison between SN 2019vxm and other SNe IIn, we constructed pseudobolometric light curves using the available photometry in the bands from B to I/i[2], excluding the UV and NIR bands where the data coverage was insufficient. The resulting evolution of the luminosity is shown in Fig. 5. The properties adopted for the comparison sample are summarised in Table D.1. Within the selected sample, most SNe IIn reach peak luminosities above 10^{43} erg s^{-1}. The peak luminosity of SN 2019vxm is $L \approx 1.59 \times 10^{43}$ erg s^{-1}, one order of magnitude higher than that of SN 2005ip ($L \approx 1.66 \times 10^{42}$ erg s^{-1}) and marginally exceeding that of SN 2010jl ($L \approx 1.39 \times 10^{43}$ erg s^{-1}). However, its luminosity remains systematically below those of the other SNe IIn in the comparison sample. SN 2019vxm is more luminous than only SN 2010jl within the comparison sample, while most objects exhibit higher peak luminosities. Nevertheless, compared with the overall population of SNe IIn, it remains towards the luminous end of the distribution ($\sim 10^{42}$–10^{44} erg s^{-1}; Kiewe et al. 2012; Taddia et al. 2013; Smith 2017; Hiramatsu et al. 2026).

[2] Specifically, SN 2003ma (B, V, I filters), SN 2005ip (B, g, V, r, i filters), SN 2006gy (B, V, r, R, i filters), SN 2006tf (B, V, R, I filters), SN 2008am (B, g, V, r, i filters), SN 2010jl (B, g, V, r, R, i, I filters), SN 2015da (B, g, V, r, R, i, I filters), SN 2017hcc (B, g, V, r, i filters), SN 2019vxm ($B, g, c, V, r, R, o, i, I$ filters).

3.5. Mid-infrared excess and dust formation

As mentioned in Sect. 3, WISE observations revealed a significant late-time excess in the IR domain. In interacting SNe, large IR emission is frequently interpreted as a signature for the presence of dust. Assuming that the source of the MIR emission is heated dust, we can estimate its mass and temperature by fitting the cool SED using simple models for graphite, silicates, and amorphous carbon composition (Fox et al. 2010). For simplicity, we assume an optically thin dust shell having mass M_d, composed by particles with radius a, and thermally emitting at a single equilibrium temperature T_d, with both M_d and T_d as free parameters. The observed flux is given by

$$F_\lambda = \frac{M_d B_\lambda(T_d)\kappa_\lambda(a)}{D^2}, \quad (1)$$

where B_λ is the Planck function for the temperature of the dust T_d, $\kappa_\lambda(a)$ is the dust opacity coefficient as a function of the wavelength for a given grain radius, and D is the distance from the observer (Hildebrand 1983). This approach has been applied to other SNe IIn (Fox et al. 2011; Stritzinger et al. 2012; Fox et al. 2013; Maeda et al. 2013; Szalai et al. 2019; Tartaglia et al. 2020). We perform our calculations for grains with size $a = 0.1\,\mu$m and $1.0\,\mu$m for both graphite and silicates chemical compositions, searching for their associated $\kappa_\lambda(a)$ values from the Mie scattering derivations presented by Fox et al. (2010)[3] (see their Fig. 4). With these assumptions, we calculated the best fits of the grey body on the MIR spectral energy distribution (SED) of SN 2019vxm estimated from *WISE* data for all available epochs. These estimates are largely uncertain owing to the SEDs being constructed from observations in only two filters in the MIR domain.

[3] Values derived from Draine & Lee (1984) and Laor & Draine (1993), recently updated by Valerin et al. (2025b). For amorphous carbon, the coefficients are taken from Colangeli et al. (1995) (see the ACAR curve in their Fig. 4).

The resulting dust masses and temperatures are summarised in Table D.3 in Appendix D. We note a general trend of increasing dust mass (a confirmation that the process of dust formation is in progress) and decreasing dust temperature between phases +6 months and +4.5 yr. At earlier phases (up to +2.5 yr), the dust masses range between 1 to 2×10^{-3} $M_\odot$. The masses are similar for different dust species, except the case of graphite with $a = 1.0\,\mu$m, whose values are one order of magnitude smaller. Given the assumption of an optically thin dust shell, the dust masses we derive must be considered as lower limits. The dust temperatures are in the range 850–1300 K (although mostly clustered on the hotter side), except for graphite with $a = 0.1\,\mu$m, which provides significantly lower temperatures, in the range 750–800 K. At later phases (between +2.5 and +3.5 yr), the dust masses are higher, $(1.4–3.3) \times 10^{-3}$ $M_\odot$, while the dust temperatures are lower (750–950 K). As a reference, Bevan et al. (2019) and Fox et al. (2010) estimated a dust mass of $(2–5) \times 10^{-3}$ $M_\odot$ for SN 2005ip at ~900 d. Finally, at the last epoch (+4.5 yr), we determine a dramatic increase in dust masses (8×10^{-3} to 0.01 $M_\odot$) and a further decrease in the dust temperature (450–600 K). The last value is close to the 0.005–0.01 $M_\odot$ found by Bevan et al. (2020) for SN 2010jl at a similar phase (+1400 days). Assuming a standard gas-to-dust ratio of 100:1 (but see Sarangi et al. 2025), the dust masses we infer imply a total CSM mass of a few tenths of $M_\odot$ and up to 1 $M_\odot$, but again these values should be considered as lower limits. We remark that our independent dust analysis is aligned with the results from Lelkes et al. (2026) but is slightly lower than the values estimated by Rameshan et al. (2026). The estimated CSM mass of SN 2019vxm is also notably lower than that of other luminous and long-lived SNe IIn, including SN 2010jl ($M_{\rm CSM} \geq 3\,M_\odot$; Fransson et al. 2014), SN 2015da ($M_{\rm CSM} = 5.5–10.3\,M_\odot$; Tartaglia et al. 2020), and SN 2017hcc ($M_{\rm CSM} \geq 10\,M_\odot$; Smith & Andrews 2020).

3.6. Light-curve modelling

We estimated the CSM properties of SN 2019vxm through the bolometric light curve using the simple analytic light-curve model presented by Moriya et al. (2013b) to reproduce the bolometric light curves of SNe powered by interaction between ejecta and dense CSM. As shown in Fig. 7, the model fits the bolometric light curve well until 100 days after peak brightness, while the model's luminosity remains systematically higher than the observed light curve at later phases. While our observations prove that an IR excess affects the bolometric light curve at phases later than 208 days, observations in the IR domain are not available at earlier stages. Consequently, an underestimated IR contribution between about 100 and 208 days can be responsible of the discrepancy between the observed bolometric light curve and the model's predictions. A similar approach was adopted for the analysis of SN 2010jl (e.g. Fransson et al. 2014; Moriya et al. 2013b; Ofek et al. 2014). Our fit resulted in $L(t) = 2 \times 10^{44} (t/\mathrm{day})^{-0.49}$ erg s^{-1}. The fitted power-law luminosity evolution is similar to those obtained for SN 2010jl ($2.04 \times 10^{44} (t/\mathrm{day})^{-0.486}$ erg s^{-1}; Moriya et al. 2013b).

If we assume that the CSM density structure follows $\rho_{\rm CSM} \propto r^{-2}$ from steady mass loss and the SN ejecta have a broken power-law density structure, $L(t) \propto t^{-0.49}$ indicates the outer SN ejecta density follows $\rho_{\rm ej} \propto r^{-8.1}$, which is consistent with the radiative envelope of LBVs (Matzner & McKee 1999). We assume that the inner SN ejecta density follows $\rho_{\rm ej} \propto r^{-1}$. Then, adopting an approach similar to that of Moriya et al. (2013b), and assuming an SN ejecta mass of 5 $M_\odot$ and an explosion energy of 5×10^{51} erg, we estimate a mass-loss rate of 0.02 $M_\odot$ yr^{-1} with the assumed CSM velocity of 60 km s^{-1}. If we set the ejecta mass to be 10 $M_\odot$, the mass-loss rate becomes 0.04 $M_\odot$ yr^{-1}. Our estimates are in agreement with the independent analysis from Rameshan et al. (2026) with their average mass-loss rate of $\dot{M} \sim 0.088\,M_\odot$ yr^{-1}, while

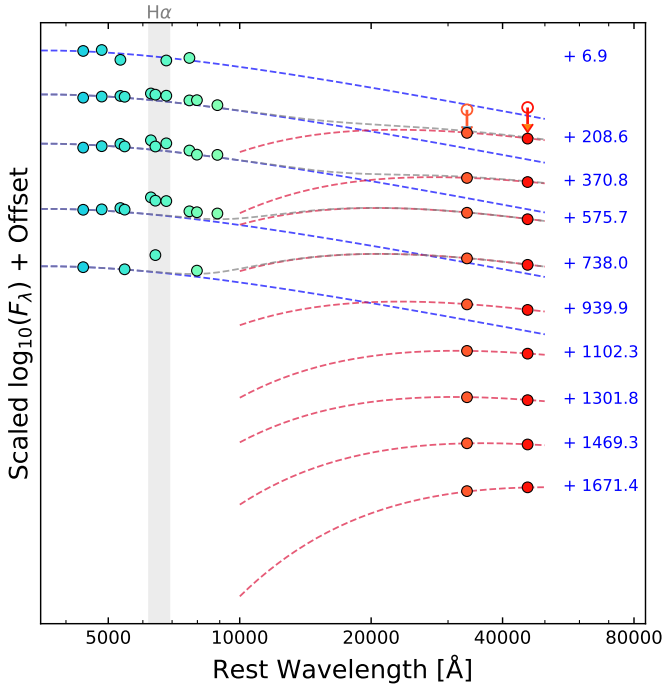


Fig. 6. Spectral energy distribution evolution of SN 2019vxm. The dashed blue lines represent the best black-body fits to the optical bands, while the dashed red lines represent the best fits of the grey-body dust emission model for silicates of $a = 0.1\,\mu$m. Each model is overplotted with the SED, and SEDs have been shifted vertically by an arbitrary constant for clarity.

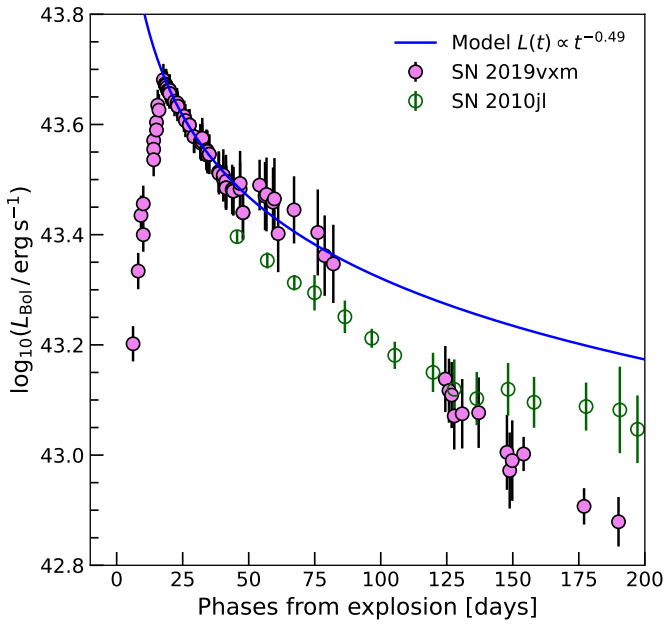


Fig. 7. Light-curve modelling of SN 2019vxm with SN 2010jl overplotted for comparison. The light curve is fitted with a single power-law function, shown as a blue line.

they are lower than the value of $\dot{M} \sim 0.2$–$1\,M_\odot\,yr^{-1}$ obtained by Lelkes et al. (2026) using an optically thick CSM model. The estimated mass-loss rate for SN 2019vxm is consistent with the value inferred from its early-phase spectrum modelling (see Sect. 4.4). This rate is also consistent with those of SN 2010jl ($\sim 0.1\,M_\odot\,yr^{-1}$; Fransson et al. 2014) and SN 2015da ($\sim 0.6\,M_\odot\,yr^{-1}$; Tartaglia et al. 2020).

4. Spectroscopy

SN 2019vxm was classified as a Type IIn SN on 2019 December 1 (Leadbeater 2019), 20.3 days prior to V-band maximum light, and just 0.7 day after the official discovery. Three days later, we started a spectroscopic follow-up campaign of SN 2019vxm, during which we collected 38 optical spectra spanning about 22 months of evolution. The data-reduction procedures applied to these spectra are outlined in Sect. A.3. The log of the spectroscopic observations is reported in Table C.1 (Appendix C), along with instrumental configuration details.

4.1. Low-resolution spectral sequence

The time series of 38 optical spectra of SN 2019vxm is shown in Fig. 8. In the following, we analyse in detail the spectral evolution during the three temporal windows identified in Sect. 3.1 (see also Table D.2). In the same three time windows, we also note major changes in the spectra of SN 2019vxm, especially in the continuum temperature and the Hα profile.

Early phases: <+100 days. The early-time spectra of SN 2019vxm are characterised by a strong blue continuum with prominent, relatively narrow Balmer emission lines (from Hα to Hδ), which are typically seen in Type IIn SNe. The obvious bump detected at ~4600–4700 Å in the first two spectra (at +14.73 and +17.68 days) is the classical flash-ionisation feature visible in a number of CC SNe, due to a blend of emission lines of C III λ4648, N III λ4640, and He II λ4686 (see the top-left panel of Fig. 13 in Sect. 4.4). In particular, these flash-ionisation signatures are frequently observed in SNe II within the first few days after the explosion (e.g. SNe 1998S, 2013fs, 2013cu, 2024cld, and PTF 11iqb; Leonard et al. 2000; Shivvers et al. 2015; Gal-Yam et al. 2014; Dessart et al. 2017; Killestein et al. 2026; Smith et al. 2015), indicating that enhanced mass loss just before the explosion is common among Type II SN progenitors (Bruch et al. 2023; Jacobson-Galán et al. 2024). However, the flash-ionisation features remained detectable in SN 2019vxm until ~17 days after the explosion. Such a long-lived flash feature is uncommon among SNe IIn and has been reported in only a handful of superluminous or strongly interacting events, such as SN 2021aaev (~37 d; Hu et al. 2026) and SN 2023gpw (≥43 d; Kangas et al. 2026). This prolonged duration suggests that the CSM environment of SN 2019vxm is highly dense, massive, and/or extended, indicating stronger mass-loss activity compared to typical SNe II. Further details are shown in the top-left panel of Fig. 13 and discussed in Sect. 4.4. In addition, we detect weak emission features of He I λ5876 and λ7065.

We estimate the temperature by fitting the continuum with a black-body function, following the methodology described by Cai et al. (2026). The best-fit results give a photospheric temperature of $T_{\rm BB} = 20\,100^{+1,450}_{-1,350}$ K for the first spectrum at +14.7 d, which then falls rapidly to $T_{\rm BB} = 14\,250^{+400}_{-350}$ K in the second spectrum (+17.7 d), and continues cooling to $T_{\rm BB} = 7400^{+100}_{-100}$ K at +76.2 d. Unfortunately, the narrowest emission components of the Balmer lines are unresolved in these early-time spectra, except for a high-resolution Copernico&Echelle spectrum at +19.7 d. However, using this spectrum, we note that both the observed Hα and Hβ profiles exhibit a narrow resolved component superimposed on a broader feature, both of which are centred at the rest wavelength. The He II λ4686 emission line is still visible in this spectrum. Detailed analysis of this Copernico&Echelle spectrum is presented in Sect. 4.2.

The other pre- and near-maximum spectra were mostly obtained with the 2.16 m Xinglong telescope (XLT) (see Table C.1 in Appendix C), and do not show significant evolution. They are just marginally redder than earlier spectra, and flash-ionisation features have completely disappeared. In all cases, the low spectral resolution does not allow for a reliable measurement of the full width at half maximum (FWHM) intensity velocity for the narrow component. The highest-quality spectrum, in terms of both signal-to-noise ratio (S/N) and resolution, was obtained with the 3 m Shane telescope at +49.1 days. The Hα profile in this spectrum is well-fitted by a two-component Gaussian function, comprising a relatively narrow emission component and a broader one. These two components were chosen purely based on their ability to accurately reproduce the observed line profile. The narrower component is unresolved, whereas the broad emission component exhibits a FWHM velocity of $2500 \pm 50\,km\,s^{-1}$ which is likely attributed to the electron-scattering wings (Huang & Chevalier 2018). After an observational gap of about one month, a new Copernico&AFOSC spectrum was obtained at +76.2 days. This spectrum is still quite blue and dominated by the unresolved Balmer components. However, a broader base in the Hα profile with a $v_{\rm FWHM} = 9500 \pm 180\,km\,s^{-1}$ is now more evident, and broad component at the blue wing of Hα rest wavelength emerged. The broad component likely originates from the high-velocity component of the ejecta, as the outer part of the CSM gradually becomes optically thin. Furthermore, the emergence of metal lines in the blue region of this spectrum suggests that some of the inner parts of the environment are gradually becoming visible. These features indicate this spectrum is transitioning towards the intermediate phases.

Intermediate phases: +100 to +400 days. The spectral monitoring of this phase starts after an observational gap of ~2 months. In this period, we note a dramatic change in the Hα and Hβ profiles: these are no longer dominated by the narrow component, as the broader component becomes progressively more prominent and exhibits an increasingly asymmetric profile. In particular, the full line profile of Hα is now reproduced with two components. The broad component has a FWHM velocity range of 6100–8400 $km\,s^{-1}$ and its centre is blueshifted by a maximum value of ~1370 $km\,s^{-1}$ with respect to the rest-frame position. Furthermore, the narrower emission is now resolved in most spectra, with a FWHM velocity range of 1200–1800 $km\,s^{-1}$ suggesting the presence of an intermediate-width component or a broadening of the previously unresolved narrow emission. The nature of this component can be clarified by analysing a higher-resolution spectrum. Specifically, we use a moderate-resolution GTC&R2500R spectrum at +166.2 d to pose tighter constraints on the wind velocity during this intermediate phase. This moderate-resolution spectrum shows a composite Hα profile, suggesting three different kinematic components: a very narrow component attributed to the unshocked CSM, an intermediate-width component due to shocked material, and a broad component produced by the SN ejecta (see Sect. 4.2). The narrow and intermediate-width components cannot be distinguished in the low-resolution spectra. In this spectrum, a narrow P Cygni feature attributed to He I λ5876 is superposed on the broad P Cygni

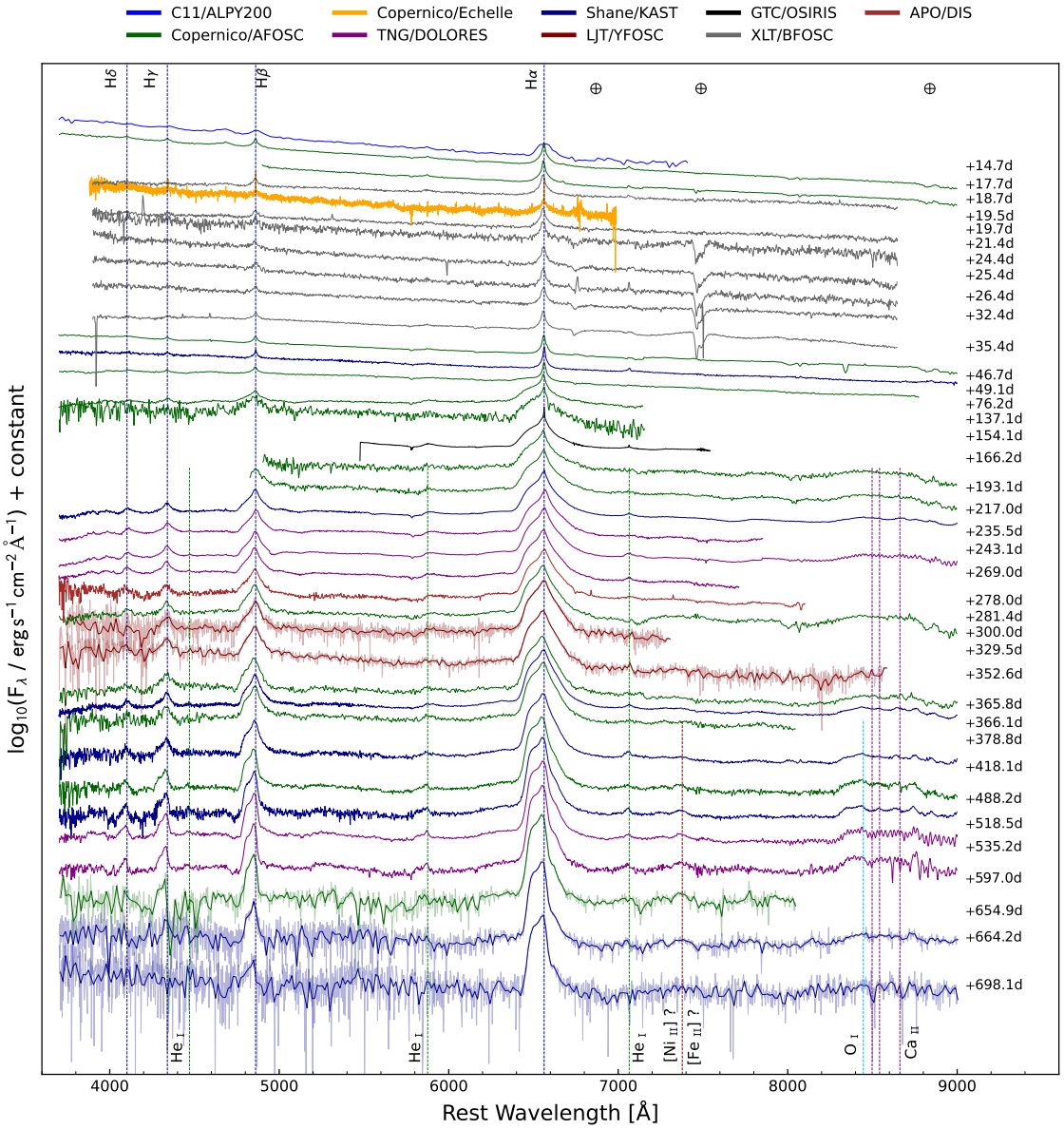


Fig. 8. Spectral evolution of SN 2019vxm. Some significant spectral features are marked with vertical coloured lines. The marked phases are with respect to the explosion epoch. The spectra have been redshift-corrected and calibrated to match the photometric data; vertical shifts have been applied for clarity. Telluric lines are indicated with encircled 'plus' symbols. Data from different telescopes and/or instruments are presented in different colours. Spectra with a low S/N were re-binned with 15 Å each bin; the original (unbinned) spectra are displayed in lighter colours behind the associated lines.

profile of Na I D, while the He I λ7065 line is observed on the red side of the spectrum (see further details in Sect. 4.2).

Subsequent spectra from +166.2 d to +378.8 d exhibit minimal evolution. Their spectral continuum is relatively red, maintaining an almost constant temperature, fluctuating between $T_{\rm BB} \approx 5650$ K and $T_{\rm BB} \approx 5150$ K. Such spectral evolution is consistent with the observed photometric evolution characterised by a sort of plateau. This behaviour is largely driven by hydrogen recombination occurring within the expanding cold dense shell (CDS). As the opacity outside the recombination front becomes negligible (Arnett & Fu 1989), the recombination process dominates this zone and produces the broad, boxy emission lines observed. Finally, these spectra confirm the presence of He I λ5876 and He I λ7065 lines; in particular, He I λ7065 is clearly detected in the high-S/N spectra and exhibits minor evolution in its profile width. Additionally, the blend between He I λ5876 and Na I D becomes more prominent with time. The blue region of the spectra exhibits a pseudocontinuum. This feature is likely caused by the line-blanketing effect within the expanding CDS, which primarily originates from metal lines such as Fe II. Finally, the systematic blueshift of the Hα lines, the asymmetry in the hydrogen-line profiles, and the IR excess observed in the light curves after +210 d, reveal the signature of new dust formation.

Late phases: >+400 days. At very late phases, the spectral continuum becomes redder and the Ca II $\lambda\lambda\lambda$8498, 8542, 8662 near-infrared (NIR) triplet becomes visible, along with He I λ5876 and He I λ7065. We noticed that the profile of He I λ7065 broadens at very late times. This suggests that the increased prominence of the blended He I λ5876 and

Na I D region is also primarily driven by the broadening of the He I λ5876 component. At very late phases, we can fit the Hα profiles with two Gaussians. The narrow component remains at a roughly constant FWHM velocity of $\sim$1300 km s^{-1}, whereas the broad component velocity gradually drops from 6950^{+270}_{-240} km s^{-1} (+294.5 d) to 3600^{+260}_{-260} km s^{-1} (+663.1 d). A broad P Cygni profile is clearly detected in the Hβ line in the +518.5 d Shane&Kast spectrum. The broad and low-contrast P Cygni absorption likely originates from the SN ejecta, exhibiting a velocity of -7100 ± 940 km s^{-1}. Additionally, we observed that the Hβ P Cygni absorption feature at +535.2 days and +597.0 days exhibits double troughs. This could be explained by the existence of a high-velocity hydrogen layer, potentially caused by an asymmetric distribution of the ejecta. However, since a corresponding feature is not observed in Hα and the blue end of the spectra suffers from a low S/N ratio, the possibility of instrumental artifacts cannot be completely ruled out. Several lines formed in the inner ejecta region, such as O I λ8446, are also detected. This indicates that the outer layers of the ejecta have gradually become optically thin, and the photosphere receded from the CDS to the inner part of the ejecta. Furthermore, we observe an emission peak around 7400 Å in our late-phase spectra. This feature is likely caused by [Fe II] and [Ni II] emission within the inner part of the ejecta. The overall spectral evolution is similar to that of other SNe IIn (e.g. SN 2017hcc; Moran et al. 2023).

In addition, as the spectral evolution progresses beyond +400 days, we note that the broad component of Hα becomes narrower, a distinct asymmetry between the blue and red wings emerges, and the peak of the broad component shows a prominent blueshift. We suggest that this morphological change might be due to dust formation. This interpretation is corroborated by the photometric data from the same period: an excess in the MIR begins to appear after $\sim$370 days (see Sect. 3.5), and the optical light curve exhibits a faster decline rate, which aligns with the obscuration and cooling effects caused by dust formation. A detailed discussion regarding the effect of dust formation on the spectroscopic observations can be found in Sect. 4.3. Additionally, Anderson et al. (2014) suggest that lines can form inside the photospheric radius derived from continuum fitting, since the opacity of the ejecta is mainly provided by electron scattering. Furthermore, the optically thick ejecta suppress emission originating from the receding regions. However, we consider this explanation less likely, as the ejecta are gradually becoming optically thin during this epoch, which is inconsistent with the assumptions made by Anderson et al. (2014).

4.2. High- and medium-resolution spectra

To constrain the velocity of the narrow component, a higher resolution spectrum is necessary. With this motivation, we obtained a high-resolution ($R \approx 20\,000$) Echelle spectrum with the Copernico 1.82 m telescope on 2019 December 06 (+19.7 d; see the fifth spectrum from the top in Fig. 8 and also in Fig. 9) where we detected symmetric Hα and Hβ profiles dominated by strong, narrow emission lines, on top of broader wings, most likely due to electron-scattering effects (Huang & Chevalier 2018). As shown in Fig. 9, a weak P Cygni absorption is detected in Hβ. The velocity inferred from the position of the minimum of the narrow Hβ absorption is -60 ± 10 km s^{-1}. Meanwhile, we clearly detect a narrow P Cygni profile in the He I λ5876 line (see Fig. 1), whose minimum is blueshifted by -60 ± 15 km s^{-1}. Hence, this is evidence of the presence of slow, unshocked CSM arising from the pre-SN wind of the progenitor. We note that

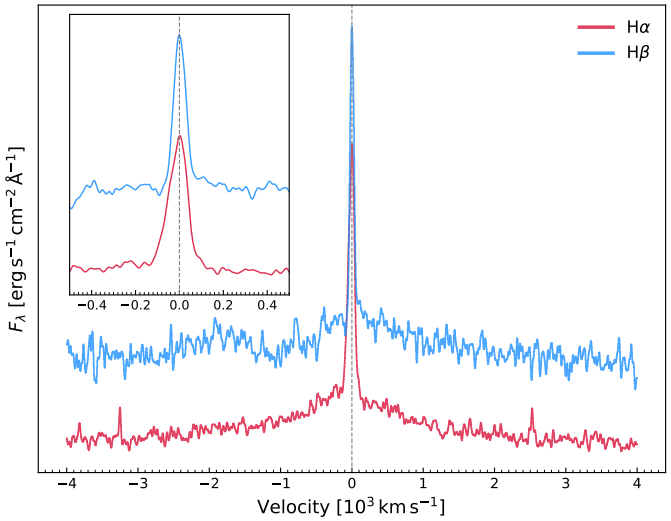


Fig. 9. Hα and Hβ profiles of SN 2019vxm (shown in red and blue colours, respectively) in velocity space, taken from the high-resolution Copernico&Echelle spectrum at +19.7 d. The inset in the upper-left corner provides a zoomed-in view of the P Cygni profiles.

wind velocities of approximately 60 km s^{-1} lie at the bottom edge of wind velocities expected in LBVs, but also at the upper limit for RSG winds (e.g. see Fig. 3 of Smith 2017).

The medium-resolution spectrum taken from GTC&R2500R at +166.2 days is shown in Fig. 10, which presents the region of the Hα line (upper panel) and the He I λ5876 line, along with the Na I D lines (lower panel). We find that the Hα profile can be described by two Gaussians and one Lorentzian (see detailed profile in the upper panel of Fig. 10). The narrowest Gaussian aligns well with the rest wavelength of Hα and shows a FWHM nearly coincident with the resolution limit ($\sim$3.4 Å; see Table C.1). This can only give an upper limit to the velocity of the unshocked CSM (<160 km s^{-1}). The intermediate component of Hα is reproduced by a Lorentzian profile, which is primarily caused by natural and collisional broadening in the dense CDS environment, showing a FWHM velocity of $\sim$1450 km s^{-1}. The broad component can be described by a Gaussian with a FWHM of $\sim$8110 km s^{-1}. This profile is suggested to form in the rapidly expanding ejecta, and the peak shows a blueshift of $\sim$25.4 Å from the rest wavelength of Hα. The blueshifted peak of the high-velocity component of Hα can be explained by the steep density profile of the ejecta and the possible formation of a CDS, which causes photons emitted from the receding side to be obscured by the optically thick material. Furthermore, since the opacity is primarily dominated by electron scattering, lines are able to form inside the photosphere (Anderson et al. 2014). As an alternative explanation, a strongly asymmetric ejection or a ^{56}Ni clump in the direction of the observer can also be invoked. However, since the dust-forming event is detected around +208.6 days, and there were no observations in MIR bands (see Sect. 3.5), the possibility of asymmetric dust absorption in the red wings of Hα cannot be entirely ruled out.

The profile of the blended He I λ5876 and Na I D lines can be described by two P Cygni profiles (see details in the lower panel of Fig. 10). We fit the profile assuming that the continuum is constant within a narrow region. The narrow double absorption trough at $\sim$5780 Å can be explained as the Galactic Na I D absorption, which shows a similar blueshift when corrected for the redshift of the SN. We suggest that the broad, low-contrast

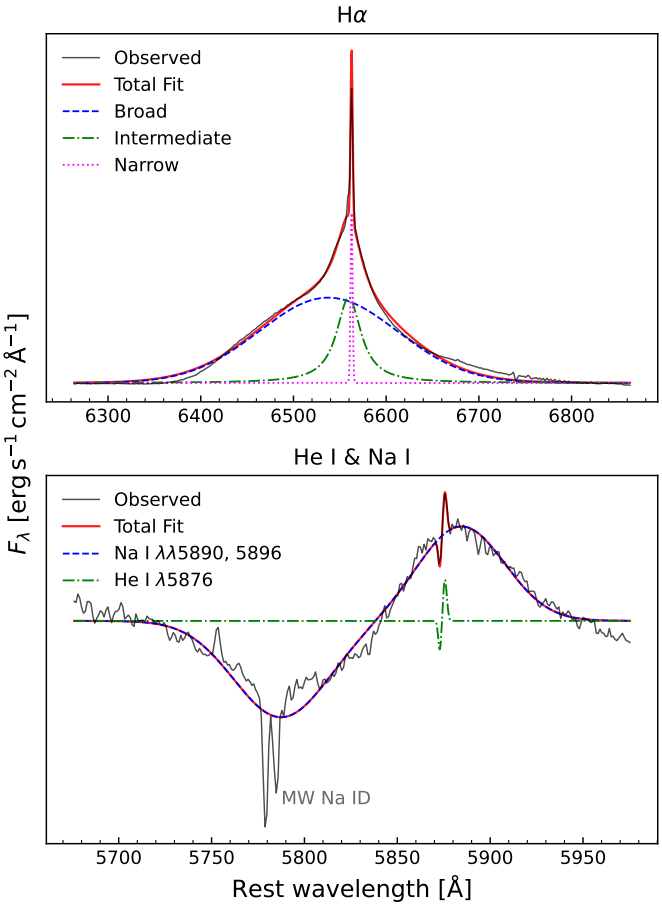


Fig. 10. Fits to the Hα, He I, and Na I profiles of SN 2019vxm taken with the medium-resolution GTC&R2500R spectrum at +166.2 d. Upper panel: Multicomponent fitting of Hα. Lower panel: Multicomponent fitting of Na I D and He I λ5876. The Na I D lines from the interstellar medium of the MW are marked. Different components are marked with different colours.

P Cygni profile might originate from the Na I D lines in the SN ejecta, exhibiting a velocity of $\sim$−5370 km s^{-1}. We note that the velocity of this profile is lower than that of the broad Hα. This difference can be explained if the velocity of Hα represents the outermost ejecta, whereas metal lines such as Na I represent the bulk velocity of the ejecta. The narrow P Cygni profile represents the He I λ5876 line. The velocity measured from the absorption component is $\sim$−160 km s^{-1}. We suggest that this profile forms in the outer unshocked CSM, since the velocity is comparable to the velocities measured from the high-resolution Hβ and He I λ5876 P Cygni profiles in the aforementioned Echelle spectrum.

4.3. Evolution of the H lines

Figure 11 presents the temporal evolution of the Hα and Hβ line profiles in the spectra of SN 2019vxm obtained from +17.7 d to +597.0 d relative to the explosion epoch. The line profiles are displayed in velocity space after the normalisation to the continuum and a vertical offset has been applied for clarity. The dashed vertical line marks zero velocity, corresponding to the rest frame.

At early epochs ($\lesssim$100 d), the symmetric Hα and Hβ profiles are well reproduced by a single Lorentzian function. The Hα and Hβ profiles during this phase are symmetric, and no significant systematic blueshift is observed. The narrow component is resolved only in the Copernico&Echelle spectrum at +19.7 d (see Sect. 4.2). We note that H emission lines undergoing electron scattering in a hot medium result in symmetric profiles, as the velocity broadening is driven by the microscopic, thermal velocities of the electrons (Münch 1948), as frequently observed in luminous SNe IIn (e.g. Smith et al. 2012; Tartaglia et al. 2020; Moran et al. 2023).

Between +100 d and +400 d, the Balmer lines undergo substantial morphological evolution. The intermediate-width component of Hα becomes more prominent and broader, and the line peak gradually shifts towards the blue. Simultaneously, the red wing is progressively suppressed, producing an increasingly asymmetric, blue-skewed profile. Hβ follows the same qualitative trend. The persistence of a strong intermediate component over several hundred days indicates sustained and powerful ejecta-CSM interaction and likely originates from the shocked material, by analogy with other long-lived Type IIn events such as SN 2010jl (Fransson et al. 2014). The systematic blueshift and attenuation of the red wing are usually interpreted as effects of the increasing optical depth due to newly formed dust within the dense post-shock region, which preferentially obscures the receding emission (Smith et al. 2008b), or intrinsic asymmetry in the CSM distribution (Fransson et al. 2014; Andrews et al. 2016).

At epochs later than +400 d, both Hα and Hβ remain clearly detectable, confirming the long-lived nature of the interaction. Although the overall widths decrease slightly compared to the peak interaction phase, the profiles retain their asymmetric, blue-dominated morphology, with a continued suppression of the red wing. Notably, dust is expected to form within the inner, metal-rich ejecta in standard Type II SNe on a one-year timescale. However, dust formation can be more efficient and occur earlier in interacting SNe. In these cases (e.g. SN 2006jc, SN 2016iog; Mattila et al. 2008; Peng et al. 2026), dust forms within the compressed CDS at the ejecta-CSM interacting interface even at earlier phases, where the high density in the radiative post-shock layers facilitate the rapid post-shock gas cooling (e.g. Smith et al. 2012; Sarangi & Slavin 2022; Dessart et al. 2025). The concurrently observed signatures of systematic blueshift and wavelength-dependent asymmetries of the Hα and Hβ emission lines (after $\sim$100 days), and IR brightening accompanied by optical fading (after $\sim$400 days), suggest new dust condensation in SN 2019vxm. Similar features have also been observed in SN 2010jl, where they were attributed to the formation of new dust (see e.g. Smith et al. 2012; Gall et al. 2014). However, Fransson et al. (2014) quantitatively interpret the blueshifted peak and symmetric Hα profiles in SN 2010jl as resulting from a scattering medium moving coherently towards the observer. Following the methodology of Fransson et al. (2014) (see also Tartaglia et al. 2020), we mirrored the red wings of the Hα profiles with respect to the computed centroid at each epoch (Fig. 12). The symmetric line profile with respect to the shifted centroid suggests that the observed blueshift of the Hα in SN 2019vxm (see Fig. 11) is also a macroscopic velocity effect.

4.4. Comparison with Type IIn SN spectra

We now compare the spectra of SN 2019vxm with those of well-observed, slowly evolving SNe IIn in four distinct phases. The upper-left panel of Fig. 13 presents a comparison of SN 2019vxm with similar SNe IIn and SLSNe-II at early phases. We selected the earliest spectrum of SN 2019vxm with adequate resolution, taken +17.7 days after the estimated explosion epoch.

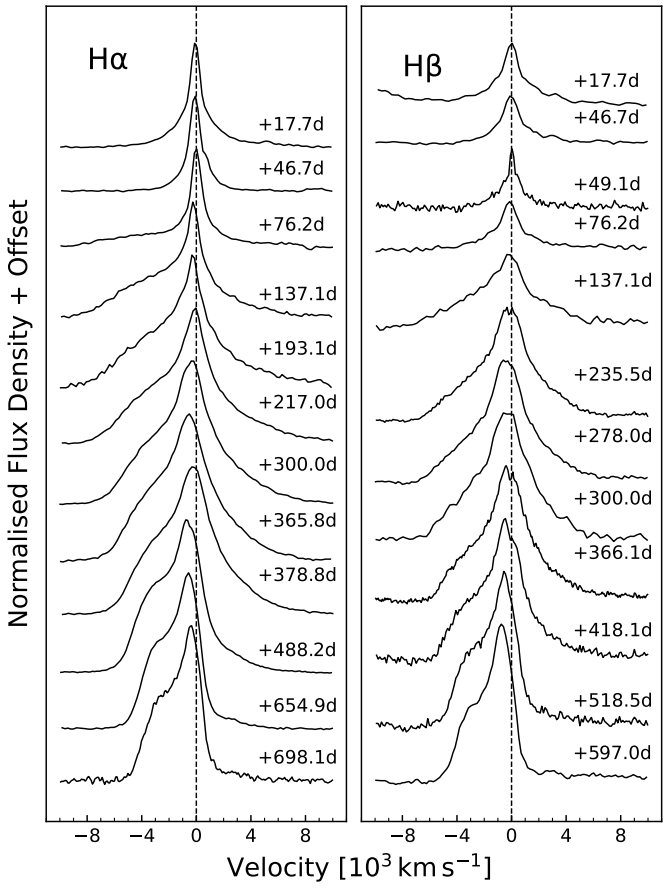


Fig. 11. Evolution of the Hα and Hβ lines of SN 2019vxm. The selected spectra exhibit a relatively high S/N and are representative of the various evolutionary phases.

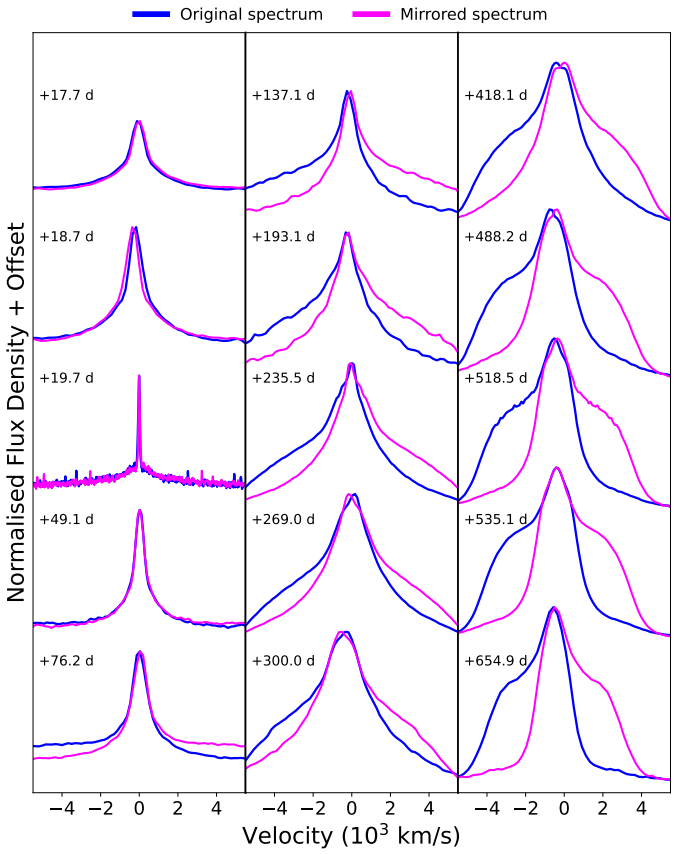


Fig. 12. Hα profiles of SN 2019vxm at selected epochs, redshifted to the line rest wavelength (blue) and mirrored with respect to the computed centroids (magenta).

At these early phases, the spectra are dominated by strong and narrow Balmer lines. High-ionisation lines, including N III and C III, are also present with moderate intensities in SN 2019vxm, suggesting that the temperature is still high at +17.7 days. In the comparison sample, only the spectrum of SN 1998S taken +3.0 days after explosion exhibits similar N III and C III flash-ionisation features. In contrast, such features are not observed in the first spectra of SN 2010jl and SN 2017hcc, while only faint C III and N III lines are tentatively identified in the spectrum of SN 2015da. The narrow emission lines of He I λ5876 and λ7065 are relatively faint compared to the Balmer lines, by analogy with other comparison objects.

To constrain the mass-loss activity of the progenitor, we compared our early-phase spectrum with early interacting SN models from Boian & Groh (2020). The theoretical models are convolved with a Gaussian kernel to match the resolution of our spectrum (~14 Å; see Table C.1). The luminosity of the model was selected to match the observed bolometric luminosity at +17.7 days after explosion, corresponding to $L \approx 10^{10}\,L_\odot$. The terminal velocity of the wind is assumed to be $v_\infty = 150\,\mathrm{km\,s^{-1}}$, which is consistent with the velocity measured from the P Cygni absorption profiles of the Hβ and He I λ5876 lines in the high-resolution spectrum. The model grid provided by Boian & Groh (2020) terminates at +3.7 days after explosion, reaching an inner radius of $R_{\rm in} \approx 3.2 \times 10^{14}$ cm. Because this theoretical phase is earlier than our first spectroscopic observation, the intensity of the prominent Balmer lines in the model is expected to be overestimated. However, because the flash-ionisation lines remain clearly visible and the derived black-body temperature remains high ($14\,260^{+370}_{-330}$ K), the physical conditions required to produce early-phase emission features are still present. Therefore, the temporal mismatch between the observation and the model does not fundamentally bias the results, and the order-of-magnitude estimation of the mass-loss rate remains physically justified.

To obtain a robust estimate of the mass-loss rate, we consider both solar and CNO-cycle abundances, which corresponds to the standard RSG and YSG progenitors. Accounting for the effects of phase mismatch, we estimate a mass-loss rate of the progenitor of $\dot{M} \gtrsim 10^{-2}\,M_\odot\,\mathrm{yr^{-1}}$ for both abundance scenarios. We consider this result as a lower limit since the actual spectroscopic epoch is later than the model assumption. This mass-loss rate is consistent with those derived for SN 2010jl ($\sim 0.1\,M_\odot\,\mathrm{yr^{-1}}$) and SN 2015da ($\sim 0.6\,M_\odot\,\mathrm{yr^{-1}}$), as reported by Fransson et al. (2014) and Tartaglia et al. (2020), respectively. The best-matching model (shown in Fig. 13 with a solid red line) exhibits Hα and Hβ line intensities comparable to those in the observed spectrum. Discrepancies primarily arise among the high-ionisation and He I lines. These inconsistencies are likely caused by the phase mismatch, as the observed line-forming region is expected to be cooler than the region in the earlier-phase model. Furthermore, the specific helium abundance or the density difference of the line-forming regions might affect the intensity of He I λ5876, but this parameter is not a critical factor for estimating the overall mass-loss rate. These results indicate a high mass-loss rate, suggesting that the progenitor of SN 2019vxm was likely an LBV or a star in a binary system

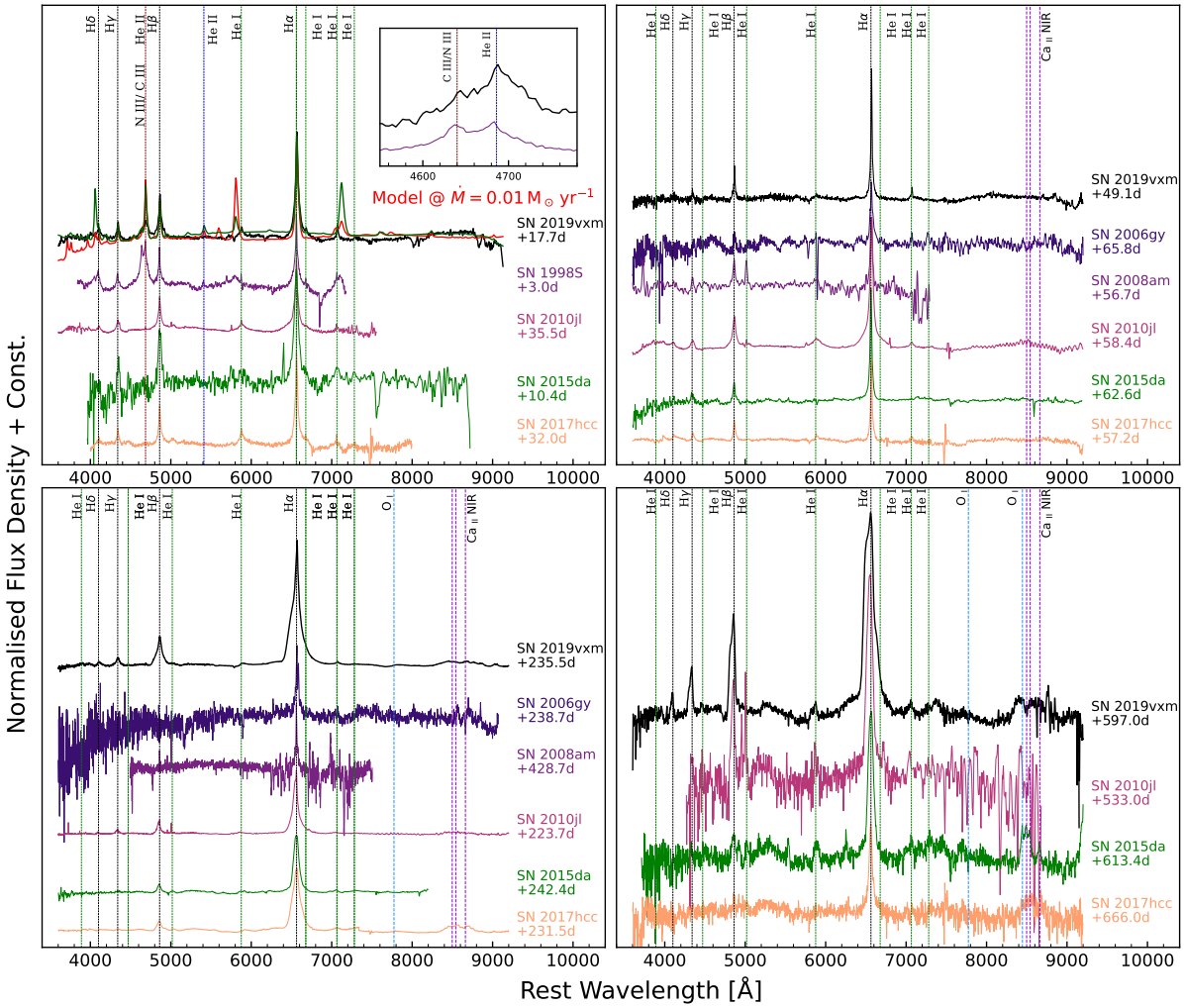


Fig. 13. Spectra of SN 2019vxm compared to similar Type IIn SNe and SLSNe-II at early (0−40 days), post-peak (40−400 days), and late phases (up to ∼600 days). Prominent spectral lines are indicated by coloured dashed lines. Phases are given relative to the estimated explosion epochs. All spectra have been redshift-corrected, dereddened, normalised, and vertically offset for clarity. In the top-left panel, a model from Boian & Groh (2020) is overplotted on an early spectrum with prominent flash-ionisation features (+17.7 days after explosion). The red line indicates the solar abundances model, while the green line denotes the CNO-Cycle abundance model. The inset shows a close-up view of the 4400–5000 Å region, highlighting the prominent flash-ionisation features.

shedding its envelope during the binary Roche-lobe overflow (RLOF) phase (see e.g. Smith 2014, 2017).

The middle, late, and very late-phase spectral comparisons are presented in the remaining three panels of Fig. 13. In the post-peak phase (40–100 days; upper-right panel), the spectra of SN 2019vxm remain dominated by strong Balmer emission lines, indicating persistent ejecta-CSM interaction (Schlegel 1990; Kiewe et al. 2012). Compared with the early phase, the continuum progressively weakens while emission features become more prominent. The Hα profile develops a broader base and shows mild asymmetry, resembling those observed in luminous SNe IIn such as SN 2010jl and SN 2015da at comparable phases (Fransson et al. 2014; Tartaglia et al. 2020). The strength of Hα relative to Hβ gradually increases; the observed Balmer decrement values are about 1.69 (+17.7 d) and 2.58 (+49.1 d), likely due to increasing optical-depth effects and possible dust attenuation in the dense post-shock region (Smith et al. 2008b; Gall et al. 2011). Helium lines, including He I λ5876 and λ7065, remain weak compared with the Balmer lines, typical of the hydrogen-rich circumstellar environments characterising normal SNe IIn (Kiewe et al. 2012; Smith 2017). The overall spectral morphology closely resembles other luminous and long-lived SNe IIn, particularly SN 2010jl, suggesting sustained interaction within dense CSM.

During the late phase (200–400 days; lower-left panel), the continuum emission further fades and the spectra become increasingly emission-line dominated. The Balmer lines remain the most prominent features; in particular, Hα exhibits pronounced intermediate and broad components similar to those seen in SNe 2005ip, 2010jl, and 2015da (Stritzinger et al. 2012; Fransson et al. 2014). The line profiles exhibit increasing asymmetry, with the red wings being gradually suppressed relative to the blue wings. Such asymmetric profiles are usually interpreted as signatures of new dust condensation in the post-shock region or anisotropic CSM geometry (Smith et al. 2008b; Andrews et al. 2016). The Ca II NIR triplet is observed in the spectrum of SN 2019vxm, as well as in SN 2006gy and SN 2017hcc.

At very late epochs ($\gtrsim$500 days; lower-right panel), SN 2019vxm continues to exhibit strong Balmer emission, confirming the long-lived nature of the interaction. The continuum becomes very faint and the spectra are dominated by

emission features. The Hα line maintains a strong, intermediate-width component and a clearly blueshifted asymmetric profile. In contrast, SN 2015da and SN 2017hcc exhibit weaker emission features at comparable epochs, suggesting less sustained CSM interaction (Tartaglia et al. 2020; Chandra et al. 2022). The Ca II NIR triplet becomes more visible at these epochs, indicating cooling ejecta and increasing importance of recombination emission. Overall, the spectral comparison indicates that SN 2019vxm belongs to the class of luminous, strongly interacting SNe IIn with long-lasting ejecta-CSM interaction, and evidence of a dense circumstellar environment shaped by intense pre-explosion mass loss and late-time dust condensation (Smith 2017; Fransson et al. 2014).

5. Discussion and conclusions

In this paper, we have presented the photometric and spectroscopic properties of SN 2019vxm, a luminous and long-lived Type IIn SN exhibiting slow spectroscopic and photometric evolution, together with an evident MIR excess at late times. SN 2019vxm shares obvious similarity with other luminous Type IIn SNe, such as SN 2010jl and SN 2017hcc, especially in terms of its overall brightness and spectral evolution.

The light curve of SN 2019vxm exhibits a relatively slow rise to the peak brightness (35.0 ± 1.8 days in the *Swift V* band), which is within the slow-rise SN IIn population of Nyholm et al. (2020). This behaviour is consistent with interaction with massive and dense CSM due to the long diffusion timescale for photons travelling through optically thick CSM. The SN is more luminous ($M_{\rm V} = -20.01 \pm 0.13$ mag) than most SNe IIn (e.g. the average peak brightness of $M_{\rm r}^{\rm peak} \approx -19.18 \pm 1.32$ mag in the sample of Nyholm et al. 2020). The estimated "optical" peak luminosity of SN 2019vxm is $L \approx 1.59 \times 10^{43}$ erg s^{-1}. The rise is followed by a monotonic decline with slow evolution (e.g. $\overline{\gamma(r)} \approx 0.55$ mag/100 d) until the SN faded below our detection threshold in the optical bands at ∼730 days after maximum light. Consequently, the follow-up campaign for SN 2019vxm was concluded at this phase. The light-curve evolution of SN 2019vxm is consistent with the findings of Nyholm et al. (2020): higher-luminosity SNe IIn are generally found to be longer-lasting, while slowly rising SNe IIn generally decline more slowly in luminosity. In addition, we examined the $B - V$ and $r - i$ colour evolution of SN 2019vxm in comparison with several SNe IIn. These objects show significant diversity in their colour behaviour over time. Such variation likely arises from differences in the physical processes that influence the thermal and radiative properties of the emitting regions.

To model the light curve of SN 2019vxm, we found a power-law decline ($L_{\rm bol} \propto t^{-0.49}$) until ∼100 days post-explosion, which is able to describe the early-time light curve, similar to SN 2010jl. The observational data deviate from the model after ∼100 days from explosion, a phenomenon potentially caused by dust formation as the ejecta cool, similar to SN 2010jl (Moriya et al. 2013b). Additionally, hydrogen recombination takes place during this phase as the temperature decreases to ∼6000 K, leading to a relatively flat evolution of the light curve, as the CDS forms and the broad Hα emission line emerges. After ∼300 days, the decline rate of the light curve becomes significantly steeper, caused by intense dust formation. A prominent MIR excess is also observed at this phase. Grey-body fitting to the SED in the MIR part suggests a lower mass limit of $\sim 10^{-4}$ M$_\odot$ for graphite dust or $\sim 10^{-3}$ M$_\odot$ for silicate dust, with temperatures of ∼1000 K. Furthermore, because the CSM interaction weakens in the late phase as the expanding CDS becomes optically thin, radioactive heating likely dominates the tail of the light curve, resulting in a faster decline that tracks radioactive decay. From the model fitting, the estimated mass-loss rates are $\dot{M} \approx 2 \times 10^{-2}$ M$_\odot$ yr^{-1} and $\dot{M} \approx 4 \times 10^{-2}$ M$_\odot$ yr^{-1} with different parameter assumptions, which are considered to be high values, supporting that there was an intense mass-loss activity decades before the explosion. However, we note that the lower bound of mass-loss rate is approximately one order of magnitude lower than the values inferred for SN 2010jl (∼0.1 M$_\odot$ yr^{-1}) and SN 2015da (∼0.6 M$_\odot$ yr^{-1}), while the upper bound is roughly consistent with these objects.

The early-time spectra of SN 2019vxm from +14.7 d to +76.2 d show very blue continua ($T \approx$ 7400–20 100 K) and prominent, narrow Balmer emission lines. The earliest two spectra are characterised by the prominent flash-ionisation features of C III, N III, and He II, from which we estimate a lower limit for the mass-loss rate of the progenitor of $\dot{M} \gtrsim 10^{-2}$ M$_\odot$ yr^{-1}. These features were also observed in the early spectra of SN 1998S (Fassia et al. 2000; Anupama et al. 2001). However, the emergence of these features in SN 2019vxm occurs at a much later epoch compared to SN 1998S. Given that the diffusion timescale in the CSM interaction is expressed as $t_{\rm CSM} \propto \kappa M_{\rm CSM}/cR_{\rm CSM}$, this long-lasting flash ionisation can be explained by massive or dense CSM. Additionally, the presence of a highly extended CSM environment cannot be ruled out. This estimate is consistent with the value inferred from the light-curve modelling and is also similar to that of SN 2010jl (see details in Sect. 3.6). The short duration (≲5 days) of these flash-ionisation features indicates that the CSM is spatially confined and originates from enhanced mass loss occurring shortly (months to a few years) before the explosion.

The Echelle spectrum may show a narrow P Cygni absorption imposed on Hβ (clearly detected in He I λ5876 line), indicative of absorption by slowly moving optically thick CSM along the line of sight with a velocity of 60 ± 10 km s^{-1}. This velocity falls marginally below the lower end of values typically inferred for LBVs (10^2–10^3 km s^{-1}; Smith et al. 2011c; Smith 2017), while it is slightly higher than velocities observed for red supergiants (RSG, 10–50 km s^{-1}; Jura & Kleinmann 1990; Smith 2017). However, the mass-loss rates inferred from both the light curve and early spectral modelling are approximately three orders of magnitude higher than typical values of RSG winds. This makes an RSG progenitor unlikely, but the rates are consistent with an LBV or binary RLOF scenario. Nevertheless, pre-SN superwinds might be occurring in RSGs (e.g. see the case of the Galactic RSG VY Canis Majoris; Smith et al. 2009b). Taken together, these lines of evidence (similar to that of SNe 2010jl and 2015da) favour a very massive star as a progenitor for SN 2019vxm, most likely an LBV. However, the possibility that the progenitor was an extreme RSG star with a superwind, or a post-RSG/LBV transitional star, cannot be entirely ruled out.

After +41.2 days, a broad emission component emerges in the Balmer lines, marking the formation of the CDS. At epochs later than +200 days post-explosion, the broad component narrows, with the FWHM velocity exhibiting a linear decline. This gradual narrowing of the profile suggests that the outer interaction region becomes increasingly optically thin, accompanied by the recession of the photosphere. Moreover, the peak of the broad component consistently exhibits a blueshift throughout the evolution. In the early phase, similar to other Type II SNe, this blueshift can be explained by line formation occurring within the photosphere radius by fitting the continuum; the probability of photon destruction is reduced in a medium where the opacity

is dominated by electron scattering (Anderson et al. 2014). In addition, increasing optical depth in the receding direction will also produce an asymmetric profile, and suppress the red-wing emission. At late phases, this asymmetric profile is likely driven by dust formation, which attenuates the red wing of the emission lines (Smith et al. 2008b; Peng et al. 2026). An asymmetric CSM distribution as in SN 2017hcc can also exhibit such features, as mentioned by Fransson et al. (2014) and Andrews et al. (2016).

Lane et al. (2026) identified the host of SN 2019vxm as a dwarf galaxy with a total stellar mass of $\log_{10}(M_g/\mathrm{M}_\odot) = 7.72^{+0.37}_{-0.55}$, consistent with the results of the environmental trends reported by Schulze et al. (2018) – SLSNe IIn are typically hosted in dwarf galaxies ($M_* \lesssim 10^{10}\,\mathrm{M}_\odot$) with only a few exceptions, such as the case of SN 2006gy. In addition, Lane et al. (2026) estimated the stellar metallicity of $\log_{10}(Z_*/Z_\odot) = -0.13^{+0.22}_{-0.26}$ for the SN host galaxy, consistent with the findings of Moriya et al. (2023) that higher mass-loss rates and wind velocities tend to occur in more metal-poor environments (also see Niu et al. 2026). This is in conflict with the expectation from radiation-driven winds, indicating that the CSM is not a result of these winds. On the other hand, Lane et al. (2026) identified a spatial and temporal coincidence between SN 2019vxm and an X-ray burst (GRB191117A) at shock breakout, finding a 3.3σ association confidence. The short duration (on the order of seconds) of the X-ray transient indicates that the interaction is most likely occurring with dense, asymmetric CSM.

Our MIR photometry of SN 2019vxm spans 7–1690 days from the explosion, and shows an IR excess starting from 210 days. At the first epoch, at a phase of ∼7 d, a single black body adequately fits the SED, but a second, cooler black body is required to reproduce the SEDs after ∼210 days (see Fig. 6 in Sect. 3.5). This reveals that there is a general trend of increasing dust mass and decreasing dust temperature with the phase. It thereby seems likely that the IR emission in SN 2019vxm originated from the newly formed dust similar to a number of other overluminous Type IIn SNe, such as SN 2010jl and SN 2017hcc.

In summary, we propose that SN 2019vxm originated from the explosion of an LBV embedded in structured, asymmetric CSM. Nevertheless, the possibility of an extreme RSG progenitor with a superwind, or a post-RSG/LBV transitional star, cannot be entirely excluded. Although SN 2019vxm was studied through multiwavelength observations, we expect further observations (particularly in the IR domain) can improve our understanding of its properties. For instance, multiband IR photometry and spectra covering multiple epochs at very late phases, combined with detailed modelling of spectral line profiles, would refine estimates of the dust properties. New spectroscopic instrumentation such as SOXS (Son Of X-Shooter; Radhakrishnan Santhakumari et al. 2024), installed on the NTT at the La Silla Observatory in Chile, will be crucial for expanding the spectral monitoring of SN 2019vxm-like events towards the NIR region. Even more, existing IR space facilities such as the James Webb Space Telescope can further extend their monitoring to longer wavelengths and to very late phases of their evolution.

Data availability

UV, optical, and MIR photometric measurements of SN 2019vxm are available at the CDS via https://cdsarc.cds.unistra.fr/viz-bin/cat/J/A+A/715/A195. Our spectra are available via the Weizmann Interactive SN Data Repository (WISeREP; Yaron & Gal-Yam 2012).

References

Anderson, J. P., Dessart, L., Gutierrez, C. P., et al. 2014, MNRAS, 441, 671
Andrews, J. E., Clayton, G. C., Wesson, R., et al. 2011, AJ, 142, 45
Andrews, J. E., Krafton, K. M., Clayton, G. C., et al. 2016, MNRAS, 457, 3241
Anupama, G. C., Sivarani, T., & Pandey, G. 2001, A&A, 367, 506
Arnett, W. D., & Fu, A. 1989, ApJ, 340, 396
Baer-Way, R., Chandra, P., Modjaz, M., et al. 2025, ApJ, 983, 101
Bevan, A., Wesson, R., Barlow, M. J., et al. 2019, MNRAS, 485, 5192
Bevan, A. M., Krafton, K., Wesson, R., et al. 2020, ApJ, 894, 111
Boian, I., & Groh, J. H. 2020, MNRAS, 496, 1325
Botticella, M. T., Pastorello, A., Smartt, S. J., et al. 2009, MNRAS, 398, 1041
Bruch, R. J., Gal-Yam, A., Schulze, S., et al. 2021, ApJ, 912, 46
Bruch, R. J., Gal-Yam, A., Yaron, O., et al. 2023, ApJ, 952, 119
Cai, Y. Z., Pastorello, A., Fraser, M., et al. 2018, MNRAS, 480, 3424
Cai, Y.-Z., Pastorello, A., Fraser, M., et al. 2021, A&A, 654, A157
Cai, Y., Reguitti, A., Valerin, G., & Wang, X. 2022, Universe, 8, 493
Cai, Y.-Z., Pastorello, A., Maeda, K., et al. 2026, A&A, 707, A157
Cappellaro, E., Botticella, M. T., Pignata, G., et al. 2015, A&A, 584, A62
Chambers, K. C., Magnier, E. A., Metcalfe, N., et al. 2016, arXiv e-prints [arXiv:1612.05560]
Chandra, P., Chevalier, R. A., James, N. J. H., & Fox, O. D. 2022, MNRAS, 517, 4151
Chatzopoulos, E., Wheeler, J. C., Vinko, J., et al. 2011, ApJ, 729, 143
Chevalier, R. A., & Fransson, C. 1994, ApJ, 420, 268
Chugai, N. N. 1997, Ap&SS, 252, 225
Chugai, N. N. 2018, MNRAS, 481, 3643
Colangeli, L., Mennella, V., Palumbo, P., Rotundi, A., & Bussoletti, E. 1995, A&AS, 113, 561
Cold, C., & Hjorth, J. 2023, A&A, 670, A48
Cutri, R. M., Wright, E. L., Conrow, T., et al. 2012, VizieR On-line Data Catalog: II/311
Dessart, L. 2024, arXiv e-prints [arXiv:2405.04259]
Dessart, L., & Hillier, D. J. 2022, A&A, 660, L9
Dessart, L., Audit, E., & Hillier, D. J. 2015, MNRAS, 449, 4304
Dessart, L., Hillier, D. J., & Audit, E. 2017, A&A, 605, A83
Dessart, L., John Hillier, D., & Sarangi, A. 2025, A&A, 698, A293
Di Carlo, E., Massi, F., Valentini, G., et al. 2002, ApJ, 573, 144
Draine, B. T., & Lee, H. M. 1984, ApJ, 285, 89
Dwarkadas, V. V. 2011, MNRAS, 412, 1639
Dwek, E., Sarangi, A., Arendt, R. G., et al. 2021, ApJ, 917, 84
Eldridge, J. J., Fraser, M., Smartt, S. J., Maund, J. R., & Crockett, R. M. 2013, MNRAS, 436, 774
Elias-Rosa, N., Pastorello, A., Benetti, S., et al. 2016, MNRAS, 463, 3894
Elias-Rosa, N., Van Dyk, S. D., Benetti, S., et al. 2018, ApJ, 860, 68
Elias-Rosa, N., Brennan, S. J., Benetti, S., et al. 2024, A&A, 686, A13
Fassia, A., Meikle, W. P. S., Vacca, W. D., et al. 2000, MNRAS, 318, 1093
Filippenko, A. V. 1982, PASP, 94, 715
Filippenko, A. V. 1989, AJ, 97, 726
Filippenko, A. V. 1997, ARA&A, 35, 309
Flewelling, H. A., Magnier, E. A., Chambers, K. C., et al. 2020, ApJS, 251, 7
Foley, R. J., Berger, E., Fox, O., et al. 2011, ApJ, 732, 32
Fox, O., Skrutskie, M. F., Chevalier, R. A., et al. 2009, ApJ, 691, 650
Fox, O. D., Chevalier, R. A., Dwek, E., et al. 2010, ApJ, 725, 1768
Fox, O. D., Chevalier, R. A., Skrutskie, M. F., et al. 2011, ApJ, 741, 7
Fox, O. D., Filippenko, A. V., Skrutskie, M. F., et al. 2013, AJ, 146, 2
Fransson, C., Ergon, M., Challis, P. J., et al. 2014, ApJ, 797, 118
Fraser, M. 2020, R. Soc. Open Sci., 7, 200467
Gall, C., Hjorth, J., & Andersen, A. C. 2011, A&ARv, 19, 43
Gall, C., Hjorth, J., Watson, D., et al. 2014, Nature, 511, 326
Gal-Yam, A., & Leonard, D. C. 2009, Nature, 458, 865
Gal-Yam, A., Leonard, D. C., Fox, D. B., et al. 2007, ApJ, 656, 372
Gal-Yam, A., Arcavi, I., Ofek, E. O., et al. 2014, Nature, 509, 471
Gangopadhyay, A. 2024, arXiv e-prints [arXiv:2411.04107]
Hildebrand, R. H. 1983, Q. J. R. Astron. Soc., 24, 267
Hiramatsu, D., Berger, E., Gomez, S., et al. 2026, ApJ, 1005, 30
Hu, Y., Lunnan, R., Pessi, P. J., et al. 2026, ApJ, 999, 176
Huang, C., & Chevalier, R. A. 2018, MNRAS, 475, 1261
Jacobson-Galán, W. V., Dessart, L., Davis, K. W., et al. 2024, ApJ, 970, 189
Jencson, J. E., Prieto, J. L., Kochanek, C. S., et al. 2016, MNRAS, 456, 2622
Jura, M., & Kleinmann, S. G. 1990, ApJS, 73, 769
Kangas, T., Charalampopoulos, P., Nagao, T., et al. 2026, A&A, 705, A52
Kankare, E., Ergon, M., Bufano, F., et al. 2012, MNRAS, 424, 855
Khazov, D., Yaron, O., Gal-Yam, A., et al. 2016, ApJ, 818, 3
Kiewe, M., Gal-Yam, A., Arcavi, I., et al. 2012, ApJ, 744, 10
Killestein, T. L., Pursiainen, M., Kotak, R., et al. 2026, MNRAS, 548, staf2261
Kochanek, C. S., Shappee, B. J., Stanek, K. Z., et al. 2017, PASP, 129, 104502
Kotak, R., & Vink, J. S. 2006, A&A, 460, L5

Lane, Z. G., Ridden-Harper, R., Rest, S., et al. 2026, ApJ, 1003, 19
Laor, A., & Draine, B. T. 1993, ApJ, 402, 441
Leadbeater, R. 2019, TNS Classif. Rep., 2019-2506
Lelkes, K., Molnár, L., Vinkó, J., et al. 2026, ApJ, submitted [arXiv:2605.23637]
Leloudas, G., Hsiao, E. Y., Johansson, J., et al. 2015, A&A, 574, A61
Leonard, D. C., Filippenko, A. V., Barth, A. J., & Matheson, T. 2000, ApJ, 536, 239
Li, W., Leaman, J., Chornock, R., et al. 2011, MNRAS, 412, 1441
Ma, X., Wang, X., Mo, J., et al. 2025a, A&A, 698, A306
Ma, X., Wang, X., Mo, J., et al. 2025b, A&A, 698, A305
Maeda, K., Nozawa, T., Sahu, D. K., et al. 2013, ApJ, 776, 5
Magnier, E. A., Chambers, K. C., Flewelling, H. A., et al. 2020, ApJS, 251, 3
Mainzer, A., Bauer, J., Cutri, R. M., et al. 2014, ApJ, 792, 30
Mattila, S., Meikle, W. P. S., Lundqvist, P., et al. 2008, MNRAS, 389, 141
Matzner, C. D., & McKee, C. F. 1999, ApJ, 510, 379
Mauerhan, J. C., Smith, N., Silverman, J. M., et al. 2013, MNRAS, 431, 2599
Miller, J. S., & Stone, R. P. S. 1993, Lick Obs. Tech. Rep., No. 66
Miller, A. A., Silverman, J. M., Butler, N. R., et al. 2010a, MNRAS, 404, 305
Miller, A. A., Smith, N., Li, W., et al. 2010b, AJ, 139, 2218
Moran, S., Fraser, M., Kotak, R., et al. 2023, A&A, 669, A51
Moriya, T. J., & Menon, A. 2024, PASJ, 76, L27
Moriya, T. J., Blinnikov, S. I., Tominaga, N., et al. 2013a, MNRAS, 428, 1020
Moriya, T. J., Maeda, K., Taddia, F., et al. 2013b, MNRAS, 435, 1520
Moriya, T. J., Tominaga, N., Langer, N., et al. 2014, A&A, 569, A57
Moriya, T. J., Stritzinger, M. D., Taddia, F., et al. 2020, A&A, 641, A148
Moriya, T. J., Galbany, L., Jiménez-Palau, C., et al. 2023, A&A, 677, A20
Münch, G. 1948, ApJ, 108, 116
Nasa Heasarc. 2014, Astrophysics Source Code Library [record ascl:1408.004]
Niu, Z., Sun, N.-C., & Liu, J. 2024, ApJ, 966, L20
Niu, Z., Sun, N.-C., Zapartas, E., et al. 2026, ApJ, 1001, 44
Nyholm, A., Sollerman, J., Tartaglia, L., et al. 2020, A&A, 637, A73
Ofek, E. O., Cameron, P. B., Kasliwal, M. M., et al. 2007, ApJ, 659, L13
Ofek, E. O., Zoglauer, A., Boggs, S. E., et al. 2014, ApJ, 781, 42
Ofek, E. O., Zackay, B., Gal-Yam, A., et al. 2019, PASP, 131, 054204
Oke, J. B., & Gunn, J. E. 1983, ApJ, 266, 713
Pastorello, A., Turatto, M., Benetti, S., et al. 2002, MNRAS, 333, 27
Pastorello, A., Reguitti, A., Morales-Garoffolo, A., et al. 2019, A&A, 628, A93
Peng, Z.-H., Benetti, S., Cai, Y.-Z., et al. 2026, A&A, 705, A104
Perley, D. A., Fremling, C., Sollerman, J., et al. 2020, ApJ, 904, 35
Prieto, J. L., Kistler, M. D., Thompson, T. A., et al. 2008, ApJ, 681, L9
Prieto, J. L., Chen, P., Dong, S., et al. 2017, Res. Notes AAS, 1, 28
Radhakrishnan Santhakumari, K. K., Battaini, F., Di Filippo, S., et al. 2024, arXiv e-prints [arXiv:2407.17288]
Rameshan, G., Teja, R. S., Sahu, D. K., et al. 2026, ApJ, submitted [arXiv:2606.25896]
Ransome, C. L., & Villar, V. A. 2025, ApJ, 987, 13
Reguitti, A., Pignata, G., Pastorello, A., et al. 2024, A&A, 686, A231
Rest, A., Foley, R. J., Gezari, S., et al. 2011, ApJ, 729, 88
Salmaso, I., Cappellaro, E., Tartaglia, L., et al. 2025, A&A, 695, A29
Sarangi, A., & Slavin, J. D. 2022, ApJ, 933, 89
Sarangi, A., Zsíros, S., Szalai, T., et al. 2025, ApJ, 993, 94
Schlafly, E. F., & Finkbeiner, D. P. 2011, ApJ, 737, 103
Schlegel, E. M. 1990, MNRAS, 244, 269
Schulze, S., Krühler, T., Leloudas, G., et al. 2018, MNRAS, 473, 1258
Sethulakshmi, V., Sutaria, F. K., Sharma, R., & Ray, A. 2026, ApJ, 1001, 169
Shahbandeh, M., Fox, O. D., Temim, T., et al. 2025, ApJ, 985, 262
Shappee, B., Prieto, J., Stanek, K. Z., et al. 2014, AAS Meet. Abstr., 223, 236.03
Shingles, L., Smith, K. W., Young, D. R., et al. 2021, TNSAN, 7, 1
Shivvers, I., Groh, J. H., Mauerhan, J. C., et al. 2015, ApJ, 806, 213
Silverman, J. M., Foley, R. J., Filippenko, A. V., et al. 2012, MNRAS, 425, 1789
Smartt, S. J. 2009, ARA&A, 47, 63
Smith, N. 2014, ARA&A, 52, 487
Smith, N. 2017, in Handbook of Supernovae, eds. A. W. Alsabti, & P. Murdin (Springer Nature Link), 403
Smith, N., & Andrews, J. E. 2020, MNRAS, 499, 3544
Smith, N., Li, W., Foley, R. J., et al. 2007, ApJ, 666, 1116
Smith, N., Chornock, R., Li, W., et al. 2008a, ApJ, 686, 467
Smith, N., Foley, R. J., & Filippenko, A. V. 2008b, ApJ, 680, 568
Smith, N., Ganeshalingam, M., Chornock, R., et al. 2009a, ApJ, 697, L49
Smith, N., Hinkle, K. H., & Ryde, N. 2009b, AJ, 137, 3558
Smith, N., Miller, A., Li, W., et al. 2010, AJ, 139, 1451
Smith, N., Li, W., Filippenko, A. V., & Chornock, R. 2011a, MNRAS, 412, 1522
Smith, N., Li, W., Miller, A. A., et al. 2011b, ApJ, 732, 63
Smith, N., Li, W., Silverman, J. M., Ganeshalingam, M., & Filippenko, A. V. 2011c, MNRAS, 415, 773
Smith, N., Silverman, J. M., Filippenko, A. V., et al. 2012, AJ, 143, 17
Smith, N., Mauerhan, J. C., Cenko, S. B., et al. 2015, MNRAS, 449, 1876
Smith, K. W., Smartt, S. J., Young, D. R., et al. 2020, PASP, 132, 085002
Smith, N., Andrews, J. E., Milne, P., et al. 2024, MNRAS, 530, 405
Spergel, D. N., Bean, R., Doré, O., et al. 2007, ApJS, 170, 377
Stanek, K. Z. 2019, TNSTR, 2019-2492, 1
Stoll, R., Prieto, J. L., Stanek, K. Z., et al. 2011, ApJ, 730, 34
Stritzinger, M., Taddia, F., Fransson, C., et al. 2012, ApJ, 756, 173
Szalai, T., Zsíros, S., Fox, O. D., Pejcha, O., & Müller, T. 2019, ApJS, 241, 38
Taddia, F., Stritzinger, M. D., Sollerman, J., et al. 2013, A&A, 555, A10
Taddia, F., Sollerman, J., Fremling, C., et al. 2015, A&A, 580, A131
Tartaglia, L., Pastorello, A., Sollerman, J., et al. 2020, A&A, 635, A39
Thévenot, M., Kabatnik, M., & Gantier, J. M. 2021, TNSAN, 212, 1
Thöne, C. C., de Ugarte Postigo, A., Leloudas, G., et al. 2017, A&A, 599, A129
Tonry, J. L., Denneau, L., Heinze, A. N., et al. 2018, PASP, 130, 064505
Tsvetkov, D. Y., Pavlyuk, N. N., Echeistov, V. A., & Baklanov, P. V. 2023, Astrophys. Bull., 78, 514
Tsvetkov, D. Y., Pavlyuk, N. N., Dodin, A. V., et al. 2024, Astron. Nachr., 345, e20230166
Turatto, M., Cappellaro, E., Danziger, I. J., et al. 1993, MNRAS, 262, 128
Valerin, G., Pastorello, A., Mason, E., et al. 2025a, A&A, 695, A43
Valerin, G., Pastorello, A., Reguitti, A., et al. 2025b, A&A, 695, A42
Vallely, P. J., Kochanek, C. S., Stanek, K. Z., Fausnaugh, M., & Shappee, B. J. 2021, MNRAS, 500, 5639
Yaron, O., & Gal-Yam, A. 2012, PASP, 124, 668
Yaron, O., Perley, D. A., Gal-Yam, A., et al. 2017, Nat. Phys., 13, 510
Zhang, T., Wang, X., Wu, C., et al. 2012, AJ, 144, 131
Zhang, X., Wang, X., Sai, H., et al. 2022, MNRAS, 509, 2013

Authors and affiliations

Y.-Z. Cai (蔡永志)[1,2,3,⋆], A. Pastorello[3], T. J. Moriya[4,5,6], X.-F. Wang (王晓锋)[1,7,⋆], A. Reguitti[3,8], A. V. Filippenko[9], L. Tomasella[3], K. Čotar[10], A. Siviero[11,3], N. Elias-Rosa[3,12], T. G. Brink[9], G. Valerin[3], S. Benetti[3], J.-W. Zhao[13], Z.-H. Peng[14,15,16], Z.-Y. Wang[15,16], I. Altunin[9,17], R. Baer-Way[9,18], E. Baron[19,20,21], V. Chander[9], M. Chu[22], A. deGraw[9], J. M. DerKacy[23], J. Isern[12,24,25], C. Jennings[9,26], R. Kotak[27], L.-P. Li[2], P. Marziani[3,28], M. May[9,29], P. A. Mazzali[30,31], A. Morales-Garoffolo[32], S. Moran[33], P. Ochner[11,3], I. Salmaso[34], L. Tartaglia[35], M. Turatto[3], H.-Y. Wu[36], D.-F. Xiang[37], S.-Y. Yan[1], J.-J. Zhang[2], and W. Zheng[9]

[1] Department of Physics, Tsinghua University, Beijing 100084, PR China
[2] International Centre of Supernovae (ICESUN), Yunnan Key Laboratory of Supernova Research, Yunnan Observatories, Chinese Academy of Sciences (CAS), Kunming 650216, China
[3] INAF – Osservatorio Astronomico di Padova, Vicolo dell'Osservatorio 5, 35122 Padova, Italy
[4] National Astronomical Observatory of Japan, National Institutes of Natural Sciences, 2-21-1 Osawa, Mitaka, Tokyo 181-8588, Japan
[5] Graduate Institute for Advanced Studies, SOKENDAI, 2-21-1 Osawa, Mitaka, Tokyo 181-8588, Japan
[6] School of Physics and Astronomy, Monash University, Clayton, VIC 3800, Australia
[7] Purple Mountain Observatory, Chinese Academy of Sciences, Nanjing 210023, PR China
[8] INAF – Osservatorio Astronomico di Brera, Via E. Bianchi 46, 23807 Merate (LC), Italy
[9] Department of Astronomy, University of California, Berkeley, CA 94720-3411, USA
[10] Flai d.o.o., Bravničarjeva ulica 13, 1000 Ljubljana, Slovenia
[11] Università degli Studi di Padova, Dipartimento di Fisica e Astronomia, Vicolo dell'Osservatorio 3, 35122 Padova, Italy
[12] Institute of Space Sciences (ICE, CSIC), Campus UAB, Carrer de Can Magrans, s/n, E-08193 Barcelona, Spain
[13] South-Western Institute for Astronomy Research, Yunnan Key Laboratory of Survey Science, Yunnan University, Kunming, Yunnan 650500, PR China
[14] School of Physics and Astronomy, Beijing Normal University, Beijing 100875, PR China
[15] School of Astronomy and Space Science, University of Chinese Academy of Sciences, Beijing 100049, China
[16] National Astronomical Observatories, Chinese Academy of Sciences, Beijing 100101, China
[17] Department of Physics, University of Nevada, Reno, NV 89557, USA
[18] Department of Astronomy, University of Virginia, 530 McCormick Road, Charlottesville, VA 22904, USA
[19] Planetary Science Institute, 1700 East Fort Lowell Road, Suite 106, Tucson, AZ 85719-2395, USA
[20] Hamburger Sternwarte, Gojenbergsweg 112, 21029 Hamburg, Germany
[21] Homer L. Dodge Department of Physics and Astronomy, University of Oklahoma, Rm 100 440 W. Brooks, Norman, OK 73019-2061, USA
[22] Department of Physics, University of California, San Diego, CA 92093, USA
[23] Space Telescope Science Institute, 3700 San Martin Drive, Baltimore, MD 21218-2410, USA
[24] Fabra Observatory, Royal Academy of Sciences and Arts of Barcelona (RACAB), 08001 Barcelona, Spain
[25] Institute for Space Studies of Catalonia (IEEC), Campus UPC, 08860 Castelldefels (Barcelona), Spain
[26] Department of Astronomy, Yale University, New Haven, CT 06520-8101, USA
[27] Department of Physics and Astronomy, University of Turku, FI-20014 Turku, Finland
[28] Instituto de Astrofísica de Andalucía, CSIC, Glorieta de Astronomía s/n, ES18008 Granada, Spain
[29] Department of Nuclear Engineering, University of Tennessee, Knoxville, TN 37996-2300, USA
[30] Astrophysics Research Institute, Liverpool John Moores University, IC2, 146 Brownlow Hill, Liverpool L3 5RF, UK
[31] Max-Planck-Institut für Astrophysik, Karl-Schwarzschild Str. 1, D-85741 Garching, Germany
[32] Department of Applied Physics, School of Engineering, University of Cádiz, Campus of Puerto Real, E-11519 Cádiz, Spain
[33] School of Physics and Astronomy, University of Leicester, University Road, Leicester LE1 7RH, UK
[34] INAF – Osservatorio Astronomico di Capodimonte, Salita Moiariello 16, 80131 Napoli, Italy
[35] INAF – Osservatorio Astronomico d'Abruzzo, Via M. Maggini snc, 64100 Teramo, Italy
[36] School of Physics and Optoelectronic, Yangtze University, Jingzhou 434023, PR China
[37] Beijing Planetarium, Beijing Academy of Sciences and Technology, Beijing 100044, PR China

⋆ Corresponding authors: yongzhi.cai@inaf.it; wang_xf@mail.tsinghua.edu.cn

Appendix A: Observations and data reduction

A.1. Finding chart of SN 2019vxm

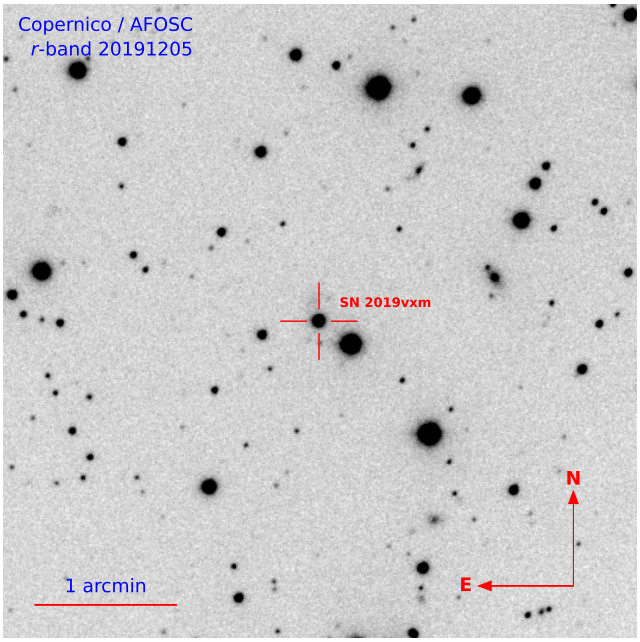


Fig. A.1. SN 2019vxm in a Copernico + AFOSC image taken with Sloan *r* filter on 2019 December 5. The SN is marked at the crosshair, near the centre of the image.

A.2. Photometric data

Soon after the discovery announcement of SN 2019vxm, we conducted a comprehensive multiband follow-up campaign in the Johnson-Cousins *UBVRI* and Sloan *ugriz* filters. The information on the instruments used are reported in Table B.1 (Appendix B).

Swift/UVOT UV and optical data were retrieved from the NASA *Swift* Data Archive[4] and measured with the standard UVOT data-reduction pipeline `HEASoft`[5] (version 6.19, Nasa Heasarc 2014). The optical photometric data obtained with ground-based telescopes were reduced with the dedicated *ecsnoopy*[6] pipeline, following standard procedures as described by Cai et al. (2018). We also collected archival data from public surveys, such as ASAS-SN, Asteroid Terrestrial-impact Last Alert System (ATLAS; Tonry et al. 2018; Smith et al. 2020; Shingles et al. 2021), and Pan-STARRS (e.g. Chambers et al. 2016; Flewelling et al. 2020; Magnier et al. 2020). ATLAS orange (*o*) and cyan (*c*) magnitudes were processed through the ATLAS Forced Photometry service[7] (Shingles et al. 2021), while Pan-STARRS1 (PS1) magnitudes were directly adopted from Lane et al. (2026). We retrieved single-exposure frames in the *W*1 (3.4 μm) and *W*2 (4.6 μm) filters from the NASA/IPAC Infrared Science Archive (IRSA), which were observed by the Near-Earth Object WISE (NEOWISE) Reactivation mission[8] (Mainzer et al. 2014). During each passage, fields often receive multiple observations over a few days, which we coadded into a single stacked image. Finally, we performed point-spread-function (PSF) fitting photometry on template-subtracted images using pre-explosion archival images obtained in May 2019. The WISE magnitudes were calibrated against the WISE All-Sky Data Release catalogue (Cutri et al. 2012). The final UV, optical, and MIR magnitudes of SN 2019vxm are published at the Strasbourg astronomical Data Centre (CDS).

A.3. Spectroscopic data

Our spectroscopy of SN 2019vxm was conducted through multiple telescopes and instruments: the 1.82 m Copernico Telescope (CT) equipped with the Asiago Faint Object Spectrograph and Camera (AFOSC) and Echelle high-resolution spectrograph, located at the Asiago Observatory, Italy; the Beijing-Faint Object Spectrograph and Camera (BFOSC) mounted on the 2.16 m Xinglong telescope (XLT) at the Xinglong Observatory, China; the Yunnan Faint Object Spectrograph and Camera (YFOSC) on the 2.4 m Lijiang telescope (LJT) at the Lijiang Observatory, China; the Kast double spectrograph (Miller & Stone 1993) mounted on the 3 m Shane telescope at Lick Observatory, USA; the Astrophysical Research Consortium (ARC) 3.5 m telescope with the Dual Imaging Spectrograph (DIS) at the Apache Point Observatory, New Mexico, USA; the Device Optimised for the LOw RESolution (DOLORES) on the 3.58 m Telescopio Nazionale Galileo (TNG), and the 10.4 m Gran Telescopio Canarias (GTC) with the Optical System for Imaging and low-Intermediate-Resolution Integrated Spectroscopy (OSIRIS); these last two telescopes are located at the Roque de los Muchachos Observatory, La Palma, Spain. In addition, we collected a single-epoch spectrum from the Transient Name Server (TNS[9]) captured at its earliest phase on 2019-12-01, which was observed by Leadbeater (2019). Basic information for the spectra of SN 2019vxm is provided in Table C.1 (Appendix C).

The Shane&Kast spectrum was obtained at or near the parallactic angle to minimise slit losses caused by atmospheric dispersion (Filippenko 1982). Its data reduction followed standard techniques for CCD frame processing and spectrum extraction (Silverman et al. 2012) using IRAF routines and custom PYTHON and IDL codes[10]. The Copernico&AFOSC spectra were processed using the dedicated pipeline `Foscgui`[11], while spectra collected from other telescopes and instruments were reduced following routine procedures within the `IRAF` environment. Specifically, raw data were first prereduced through preliminary tasks, including bias subtraction, overscan correction, trimming, and flat-fielding. One-dimensional (1D) spectra were then optimally extracted from the 2D frames. Flux and wavelength calibrations were performed using spectra from spectrophotometric standard stars and comparison lamps, respectively. Subsequently, the strongest telluric absorption bands (e.g. H_2O and O_2) in the SN spectra were removed using the spectra of standard stars. Finally, the spectral flux was fine-tuned by comparing it with coeval broad-band photometry.

[4] https://heasarc.gsfc.nasa.gov/cgi-bin/W3Browse/swift.pl
[5] https://heasarc.gsfc.nasa.gov/lheasoft/download.html
[6] *ecsnoopy* is a package for SN photometry using PSF fitting and/or template subtraction developed by E. Cappellaro. A package description can be found at https://sngroup.oapd.inaf.it/ecsnoopy.html.
[7] https://fallingstar-data.com/forcedphot/
[8] While Thévenot et al. (2021) report that NEOWISE-R detected SN 2019vxm, we were not able to retrieve their measurements; therefore, we performed our own analysis of the original data.
[9] https://www.wis-tns.org/object/2019vxm
[10] https://github.com/ishivvers/TheKastShiv
[11] https://sngroup.oapd.inaf.it/foscgui.html

Appendix B: Photometric facilities

Table B.1. Information on the instrumental setups.

Code	Diameter (m)	Telescope	Instrument	Filters	Site
Moravian	0.67/0.92	Schmidt Telescope	Moravian	*uBVgri*	Osservatorio Astronomico di Asiago, Asiago, Italy
Andor	0.80	Tsinghua-NAOC Telescope (TNT)	Andor DZ936	*Bgri*	Xinglong Observatory, Hebei, P.R. China
LAIA	0.80	Joan Oró Telescope (TJO)	LAIA	*UBVRI*	Montsec Astronomical Observatory, Catalonia, Spain
Nickel	1.02	Nickel Telescope	Nickel	*BVRI*	Lick Observatory, California, USA
AFOSC	1.82	Copernico 1.82m Telescope	AFOSC	*BVgriz*	Osservatorio Astronomico di Asiago, Asiago, Italy
IO:O	2.00	Liverpool Telescope (LT)	IO:O	*uBVgriz*	Observatorio Roque de Los Muchachos, La Palma, Spain
LJT	2.40	Lijiang 2.4 m Telescope	YFOSC	*BVgri*	Gaomeigu site, Lijiang Observatory (LJO), Yunnan, P.R. China
ALFOSC	2.56	Nordic Optical Telescope	ALFOSC	*BVgriz*	Observatorio Roque de Los Muchachos, La Palma, Spain
ATLAS	0.50	ATLAS	ATLAS	*co*	Haleakalā Observatory and Mauna Loa Observatory, Hawaii, USA
PS1	1.80	Pan-STARRS1	GPC1	*i*	Haleakalā Observatory, Maui, Hawaii, USA
UVOT	0.30	*Swift* Modified Ritchey-Chrétien	UVOT	*UV* filters+*ubv*	*Neil Gehrels Swift Observatory*
WISE	0.40	Wide-field Infrared Survey Explorer	WISE	*W*1 + *W*2	*Wide-field Infrared Survey Explorer*

Appendix C: Log of spectroscopic observations

Table C.1. Log of the spectroscopic observations of SN 2019vxm.

Date	MJD	Phase[a] (d)	Instrumental setup	Grism/Grating	Spectral range (Å)	Exposure time (s)	Resolution (Å)
2019-12-01	58818.73	+14.73	C11+ALPY200	200 mm^{-1}	3550–7440	4200	$R \approx 130$
2019-12-04	58821.68	+17.68	Copernico+AFOSC	VPH7+6	3150–9290	1500	15
2019-12-05	58822.70	+18.70	Copernico+AFOSC	VPH7+6	4990–9290	1500	15
2019-12-06	58823.48	+19.48	XLT+BFOSC	G4	3940–8810	2400	$R \approx 350$
2019-12-06	58823.73	+19.73	Copernico+ECHELLE	300	3840–7150	3600	$R \approx 20,000$
2019-12-08	58825.41	+21.41	XLT+BFOSC	G4	3970–8810	2400	$R \approx 350$
2019-12-10	58827.41	+23.41	XLT+BFOSC	G4	3950–8810	3000	$R \approx 350$
2019-12-11	58828.42	+24.42	XLT+BFOSC	G4	3970–8810	3000	$R \approx 350$
2019-12-12	58829.43	+25.43	XLT+BFOSC	G4	3980–8810	3000	$R \approx 350$
2019-12-13	58830.43	+26.43	XLT+BFOSC	G4	3970–8810	3000	$R \approx 350$
2019-12-19	58836.44	+32.44	XLT+BFOSC	G4	3970–8810	3000	$R \approx 350$
2019-12-22	58839.45	+35.45	XLT+BFOSC	G4	3970–8810	3000	$R \approx 350$
2020-01-01	58849.44	+45.44	XLT+BFOSC	G4	3970–8810	3000	$R \approx 350$
2020-01-02	58850.72	+46.72	Copernico+AFOSC	VPH7+6	3390–9290	1800	15
2020-01-05	58853.10	+49.10	Shane+Kast	4310/7500	3620–10700	1680	9
2020-02-01	58880.16	+76.16	Copernico+AFOSC	VPH7+6	3450–8940	1800	15
2020-04-02	58941.09	+137.09	Copernico+AFOSC	VPH7	3420–7280	1800	14
2020-04-19	58958.13	+154.13	Copernico+AFOSC	VPH7	3700–7290	600	14
2020-05-01	58970.20	+166.20	GTC+OSIRIS	R2500R	5590–7680	900	3.4
2020-05-28	58997.09	+193.09	Copernico+AFOSC	VPH6	5000–9300	1500	15
2020-06-21	59021.03	+217.03	Copernico+AFOSC	VPH7+6	3450–7290	600	15
2020-07-09	59039.46	+235.46	Shane+Kast	4310/7500	3620–10710	2760/2700	9
2020-07-17	59047.10	+243.10	TNG+DOLORES	LRB	3300–8000	900	11
2020-08-12	59073.00	+269.00	TNG+DOLORES	LRB+LRR	3220–10000	1200	11
2020-08-21	59082.03	+278.03	TNG+DOLORES	LRB	3110–7860	1200	11
2020-08-24	59085.38	+281.38	ARC+DIS	B400+R300	3750–8260	3000/3000	13
2020-09-12	59104.01	+300.01	Copernico+AFOSC	VPH7+6	3700–9300	1200	15
2020-10-11	59133.52	+329.52	LJT+YFOSC	G14	3810–7440	2100	15
2020-11-03	59156.59	+352.59	LJT+YFOSC	G14	3490–8740	2100	15
2020-11-16	59169.81	+365.81	Copernico+AFOSC	VPH7+6	3600–9300	1200	15
2020-11-17	59170.10	+366.10	Shane+Kast	4310/7500	3620–10700	2460/2400	9
2020-11-29	59182.76	+378.76	Copernico+AFOSC	Gr4	3400–8200	1500	14
2021-01-08	59222.10	+418.10	Shane+Kast	4310/7500	3620–10700	2160/2220	9
2021-03-19	59292.20	+488.20	Copernico+AFOSC	Gr4	3600–9670	1200	14
2021-04-18	59322.50	+518.50	Shane+Kast	4310/7500	3630–10700	3660/3600	9
2021-05-05	59339.15	+535.15	TNG+DOLORES	LRB+LRR	3550–10380	1200	12
2021-07-06	59401.02	+597.02	TNG+DOLORES	LRB+LRR	3310–10250	2700	12
2021-09-01	59458.86	+654.86	Copernico+AFOSC	Gr4	3580–8200	3600	14
2021-09-11	59468.20	+664.20	Shane+Kast	4310/7500	3630–10760	3360/3300	9
2021-10-15	59502.14	+698.14	Shane+Kast	4310/7500	3620–10270	3660/3600	9

[a]Phases are relative to explosion epoch (MJD = 58804.0) in the observer frame.

Appendix D: Supplementary materials

Table D.1. Basic information of the sample SNe.

Object	Explosion Epoch [MJD]	Peak Epoch [MJD]	Peak Mag.† [mag]	$L_{\rm peak}$ [erg s^{-1}]	Redshift z	Distance [Mpc]	$E(B-V)_{\rm MW}$ [mag]	$E(B-V)_{\rm Host}$ [mag]	Source
SN 2003ma	52971	52992	~ -22.2	5.78×10^{43}	0.289	1534	0.348	~ 0	1
SN 2006gy	53967	54035	~ -22.4	5.94×10^{43}	0.019	76 ± 14	0.16	~ 0.54	4,5
SN 2006tf	–	54112	~ -21.1	2.39×10^{43}	0.074	346	0.027	~ 0	6
SN 2008am	54438.8 ± 1	54505	~ -21.3	9.02×10^{43}	0.2338	1205	0.025	~ 0	7
SN 2010jl	55470	55494	~ -19.4	1.39×10^{43}	0.0107	49	0.027	~ 0	8
SN 2014ab	~ 56625.4	≤ 56671.1	≤ -19.1	1.00×10^{43}	0.02262	94.3	0.027	~ 0	9
SN 2015da	57030.95	57131	~ -20.0	2.19×10^{43}	0.006669	32.1	0.01	0.97 ± 0.27	10,11
SN 2017hcc	58027.4 ± 1	58084	~ -21.0	3.96×10^{43}	0.0168	77.57	0.029	$\lesssim 0.016$	12
SN 2019vxm	58804	58839	~ -20.3	1.59×10^{43}	0.019	79.2 ± 4.2	0.087 ± 0.002	~ 0	This work

NOTE: Sources: 1 = Rest et al. (2011); 4 = Ofek et al. (2007); 5 = Smith et al. (2007); 6 = Smith et al. (2008a); 7 = Chatzopoulos et al. (2011); 8 = Ofek et al. (2014); 9 = Moriya et al. (2020); 10 = Smith et al. (2024); 11 = Tartaglia et al. (2020); 12 = Moran et al. (2023). †: The peak magnitudes are obtained from the optical bands with best coverage.

Table D.2. Decline rates (in mag /100 d) of the multiband light curves of SN 2019vxm.

Filter	γ_{0-100}	$\gamma_{100-400}$	$\gamma_{400-700}$
u	1.70 ± 0.03	0.66 ± 0.02	–
U	1.95 ± 0.09	–	–
B	1.32 ± 0.03	0.64 ± 0.02	1.35 ± 0.05
g	1.14 ± 0.04	0.60 ± 0.01	1.38 ± 0.03
c	–	0.56 ± 0.03	1.24 ± 0.09
V	1.06 ± 0.04	0.56 ± 0.02	1.28 ± 0.02
r	0.61 ± 0.03	0.25 ± 0.01	0.83 ± 0.03
o	0.47 ± 0.01	0.34 ± 0.01	1.02 ± 0.03
i	0.59 ± 0.05	0.58 ± 0.01	1.09 ± 0.02
z	0.61 ± 0.03	0.55 ± 0.02	1.10 ± 0.02
Filter		$\gamma_{600-800}$	
R		0.83 ± 0.03	
I		1.21 ± 0.04	
Filter		γ_{0-40}	
$UVW1$		3.48 ± 0.11	
$UVM2$		4.55 ± 0.13	
$UVW2$		4.96 ± 0.11	
Filter		$\gamma_{1000-1700}$	
$W1$		0.24 ± 0.03	
$W2$		0.12 ± 0.03	

Table D.3. Dust properties at different phases since the explosion epoch.

MJD	Phase	Standard Black Body		Graphite $a = 0.1\,\mu$m		Graphite $a = 1.0\,\mu$m	
		R (AU)	T (K)	M_d ($M_\odot$)	T (K)	M_d ($M_\odot$)	T (K)
59012.58	208.6	1486	1296	1.05×10^{-3}	767	1.20×10^{-4}	1210
59174.82	370.8	1926	1059	1.64×10^{-3}	684	1.98×10^{-4}	1003
59379.77	575.7	1685	1447	1.42×10^{-3}	812	1.55×10^{-4}	1338
59542.04	738.0	1471	1429	1.08×10^{-3}	807	1.18×10^{-4}	1323
59743.89	939.9	1518	1267	1.09×10^{-3}	758	1.25×10^{-4}	1185
59906.32	1102.3	2302	935	2.26×10^{-3}	632	2.81×10^{-4}	892
60105.86	1301.8	1838	950	1.44×10^{-3}	639	1.79×10^{-4}	906
60273.36	1469.3	2234	817	2.06×10^{-3}	578	2.63×10^{-4}	785
60475.46	1671.4	4629	594	8.54×10^{-3}	458	1.12×10^{-3}	577
MJD	Phase	Amorph. Carbon		Silicates $a = 0.1\,\mu$m		Silicates $a = 1.0\,\mu$m	
		M_d ($M_\odot$)	T (K)	M_d ($M_\odot$)	T (K)	M_d ($M_\odot$)	T (K)
59012.58	208.6	9.62×10^{-5}	942	1.44×10^{-3}	1102	9.57×10^{-4}	994
59174.82	370.8	1.53×10^{-4}	816	2.34×10^{-3}	930	1.53×10^{-3}	854
59379.77	575.7	1.28×10^{-4}	1013	1.89×10^{-3}	1204	1.27×10^{-3}	1074
59542.04	738.0	9.74×10^{-5}	1004	1.44×10^{-3}	1192	9.65×10^{-4}	1065
59743.89	939.9	9.97×10^{-5}	927	1.49×10^{-3}	1081	9.93×10^{-4}	978
59906.32	1102.3	2.14×10^{-4}	743	3.30×10^{-3}	835	2.14×10^{-3}	774
60105.86	1301.8	1.36×10^{-4}	752	2.10×10^{-3}	847	1.37×10^{-3}	784
60273.36	1469.3	1.97×10^{-4}	668	3.07×10^{-3}	741	1.98×10^{-3}	693
60475.46	1671.4	8.22×10^{-4}	513	1.30×10^{-2}	553	8.31×10^{-3}	527

Appendix E: Acknowledgements

We thank the anonymous referee for his/her insightful comments and suggestions that improved the paper. This work is supported by the National Natural Science Foundation of China (NSFC grants 12288102, 12303054, 12033003, 11633002), the Yunnan Fundamental Research Projects (grants 202401AU070063, 202501AS070078), the National Key Research and Development Program of China (grant 2024YFA1611603), and the International Centre of Supernovae, Yunnan Key Laboratory (No. 202505AV340004). Y.-Z.C., A.R., I.S., and G.V. acknowledge financial support from the SOXS project (PI S. Campana). A.P., A.R., N.E.R., L.T., G.V., and S.B. acknowledge support from the PRIN-INAF 2022, "Shedding light on the nature of gap transients: from the observations to the models." X.-F.W. is also supported by the Tencent Xplorer Prize. S.M. is funded by Leverhulme Trust grant RPG-2023-240. J.I. acknowledges funding by Spanish program Unidad de Excelencia María de Maeztu CEX2020-001058-M, PID2023-149918NB-I00, and 2021-SGR-1526 (Generalitat de Catalunya). P.M. acknowledges financial support from the Spanish MCIU through project PID2022-140871NB-C21 by "ERDF A way of making Europe," and from the Severo Ochoa grant CEX2021-515001131-S funded by MCIN/AEI/10.13039/501100011033. A.M.G. acknowledges financial support from grant PID2023-152609OA-I00, funded by the Spanish Ministerio de Ciencia, Innovación y Universidades (MICIU), the Agencia Estatal de Investigación (AEI 10.13039/501100011033), and the European Union's European Regional Development Fund (ERDF). A.V.F.'s research group at UC Berkeley acknowledges financial assistance from the Christopher R. Redlich Fund, Gary and Cynthia Bengier, Clark and Sharon Winslow, Alan Eustace and Kathy Kwan (W.Z. is a Bengier-Winslow-Eustace Specialist in Astronomy), Timothy and Melissa Draper, Briggs and Kathleen Wood, Ellyn and Alan Seelenfreund (T.G.B. is Draper-Wood-Seelenfreund Specialist in Astronomy), and numerous other donors.

This article is based in part on observations made with the Italian Telescopio Nazionale Galileo (TNG), operated on the island of La Palma by the Fundación Galileo Galilei of the INAF (Istituto Nazionale di Astrofisica) at the Spanish Observatorio del Roque de los Muchachos of the Instituto de Astrofísica de Canarias, under program A50TAC_41 (PI G. Valerin). Based in part on observations made with the Gran Telescopio Canarias (GTC; Program 98-GTC69/20A) installed at the Spanish Observatorio del Roque de los Muchachos of the Instituto de Astrofísica de Canarias, on the island of La Palma. Based in part on observations collected at Copernico and Schmidt telescopes (Asiago Mount Ekar, Italy) of the INAF – Osservatorio Astronomico di Padova. A major upgrade of the Kast spectrograph on the Shane 3 m telescope at Lick Observatory, led by Brad Holden, was made possible through gifts from the Heising-Simons Foundation, William and Marina Kast, and the University of California Observatories. Research at Lick Observatory is partially supported by a gift from Google. We appreciate the expert assistance of the staff at the various observatories where data were obtained. We acknowledge the use of public data from the ATLAS, Pan-STARRS, ZTF, Swift, and WISE data archive. We thank T. Zwitter, M. Fiaschi, Z.-H. Chen, F.-Z. Guo, Z.-T. Li, J. Mo, T. Chapman, S. Modak, D. Punjabi, J. Sunseri, K. Bostow, N. Girish, S. Kumar, E. Liu, E. Ma, E. McGinness, A. Parke, and A. Yagubyan for their help with the observations and data reduction for SN 2019vxm.